DESIGN OF COMPACT EVAPORATORS FOR ULTRA LOW TEMPERATURE THERMAL MANAGEMENT OF MICROPROCESSORS

A Thesis
Presented to
The Academic Faculty

By

Robert Paul Wadell

In Partial Fulfillment
of the Requirements for the Degree
Master's of Science in Mechanical Engineering

Georgia Institute of Technology
August 2005

DESIGN OF COMPACT EVAPORATORS FOR ULTRA LOW TEMPERATURE THERMAL MANAGEMENT OF MICROPROCESSORS

Approved:

Yogendra Joshi, Ph.D., Chair
Department of Mechanical Engineering
Georgia Institute of Technology

Andrei Fedorov, Ph.D., Co-Advisor
Department of Mechanical Engineering
Georgia Institute of Technology

Paul Kohl, Ph.D.
Department of Chemical Engineering
Georgia Institute of Technology

Date Approved: 7/13/05

To my future wife

Paula Marie Weinstein

ACKNOWLEDGEMENTS

I would like to thank Dr. Yogendra Joshi and Dr. Andrei Fedorov for their technical mentoring, direction, and support during this research. I would also like to thank Dr. Paul Kohl for his technical review and support as a member on my thesis committee. I would like to thank the mechanical, electrical, and chemical engineering students and professors of the IFC thermal task group for the experience of working with them on confronting the current and future thermal management challenges facing the microprocessor design community. I would like to thank the members of the Microelectronics and Emerging Technologies Thermal Laboratory, in particular Dr. Stephane Launay, Dr. Xiaojin Wei, Dr. David Gerlach, and Scott Wilson for their insight and feedback during my work. I thank my fiancé Paula Weinstein for her constant and enduring support and encouragement through my research, especially in the early months of my work and adaptation to graduate school. I would like to thank my friends Adam Christensen, John Berg, Scott Driscoll, for making my social life in graduate school a much more exciting experience. I would like to thank Regina Neequaye for her administrative experience and John Graham from the machine shop for his feedback in machining techniques. Finally, I would like to thank the Interconnect Focus Center at the Georgia Institute of Technology for the graduate fellowship and research funding.

TABLE OF CONTENTS

LIST OF TABLES

LIST OF FIGURES

NOMENCLATURE

Symbols

A	Area (m^2)
a	Number of active blocks in microprocessor
A_w	Heated surface area of channels/pin fins (m^2)
C_{ave}	Average capacitance (Farad)
C_c	Coefficient of contraction
CHF	Critical heat flux (W/m^2)
d_h	Hydraulic diameter (m)
f	Frequency of microprocessor (s^{-1})
f_l	Liquid friction factor
G	Mass flux (kg/m^2s)
g	Gravity (m/s^2)
h_{eff}	Effective heat transfer of evaporator (W/m^2K)
h_{tp}	Two-phase heat transfer coefficient between wall and refrigerant (W/m^2K)
H	Enthalpy (J/kg K)
H_{ch}	Height of micro-channel (m)
H_{tc}	Distance from thermocouple to the base of the channel (m)
I_{in}	Current drawn from cartridge heaters (Amperes)
$I_{leakage}$	Leakage current (Amperes)
k	Thermal conductivity (W/mK)

L	Length (m)
m	Fin parameter (m^{-1})
$\dot{m}$	Mass flow rate (kg/s)
Ma	Mach number
N	Parameter used in Shah correlations
N_{data}	Number of data points
N_{tr}	Number of transistors in microprocessor
P	Pressure (bar)
ΔP	Pressure Drop (bar)
P_e	Total power of microprocessor (W)
Q_{HL}	Heat leak into evaporator from ambient (W)
Q_{in}	Heat delivered to evaporator from cartridge heaters (W)
q”	Heat flux (W/m^2), unless specified
$q”_w$	Heat flux at wetted wall of microstructures (W/m^2)
V_{dd}	Supply voltage to microprocessor (V)
V_{in}	Voltage supplied to cartridge heaters (V)
u	Velocity (m/s)
W	Width (m)
W_w	Width of wall in unit cell (m)
T	Temperature (^oK or ^oC)
x_e	Thermodynamic equilibrium quality
z	Stream-wise location (m)

Greek and Roman Characters

α	Void fraction
ϕ_l	Two phase friction multiplier
Ω	Angle with horizontal (radians)
ρ	Density (kg/m^3)
Λ	Compressibility factor
μ	Viscosity (kg/ms)
η	Fin efficiency
σ	Surface tension (N/m)
v	Specific volume (m^3/kg)
$\dot{\forall}$	Volumetric Flow Rate (m^3/s)
ψ	Dimensionless number used in Lee and Lee correlation

Subscripts

acc	Accelerational
av	Average
b	Base
c	Constriction
ch	Channel
chip	Chip/microprocessor, or referring to surface of heater block
drop	Drop
e	Expansion
i	Inlet

o	Outlet
f	Liquid
fr	Frictional
g	Gas
grav	Gravitational
m	Measured
max	Maximum
s	Solid (copper)
sat	Saturation
w	Wall
W	Location W, 2 mm from entrance in steam-wise direction
Y	Location Y, 6 mm from entrance in steam-wise direction
Z	Location Z, 8 mm from entrance in steam-wise direction
1	State 1 – Before Low Stage Compressor
2	State 2 – After Low Stage Compressor
3	State 3 – Before Low Stage Condenser
4	State 4 – After Low Stage Condenser
5	State 5 – Before Low Stage Evaporator
6	State 6- After Low Stage Evaporator

SUMMARY

It is well known that microprocessor performance can be improved by lowering the junction temperature. Two-stage cascade vapor compression refrigeration (VCR) is a compact, inexpensive, reliable, and simpler technology that can achieve temperatures close to –100 ^{o}C. Recent analytical studies have shown that for a power limited chip, there is a non-linear scaling effect that offers a 4.3X performance enhancement at –100 ^{o}C, compared to 85 ^{o}C operation. The current study is an experimental investigation of high heat flux low temperature evaporators that interface the microprocessor to a cascaded VCR system. Four compact evaporator designs are evaluated - a baseline case with no enhancement structures, micro channels, inline pin fin arrays, and alternating pin fin arrays. A two-stage R134a/R508b cascade refrigeration system provides refrigerant (R508b) to the evaporator at flow rates of 50 - 70 g/min and saturation temperatures of -86 ^{o}C to –79 ^{o}C. Pressure drop and heat transfer measurements are used to explain the performance of the four geometries, for the range of heat fluxes of 20-100 W/cm^2. The boiling curves are highly dependent on mass flow rate, indicating that forced convective heat transfer due to annular flow is the main heat transfer mechanism. Flow visualization of boiling in micro-channels confirms that the flow is annular. The alternating pin fin geometry offered the best performance, maintaining a maximum chip temperature of –62.6 ^{o}C at 100 W/cm^2. Even though the pin fins and micro-channels maintained lower chip temperatures than the baseline geometry with no enhancement structures at a given heat flux, the performance improvement was due to an increase in surface area, and not the heat transfer coefficient between the refrigerant and wall.

INTRODUCTION

1.1 Background

Over the past decade performance of laptop, desktop, and server computers has undergone vast improvements due to miniaturization of CMOS technology. However, in order to meet this functionality, heat dissipation rates have increased at an alarming rate [1]. Alternatives to air cooling, such as pool boiling based thermosyphons and heat pipes, are currently being explored that can accommodate the high heat flux and temperature uniformity demands of the microprocessor industry.

At the same time, sub-ambient cooling technologies have been employed to offer increases in chip processing power and reliability by lowering the junction temperature [2-6], while still meeting high heat flux and temperature uniformity demands. Due to a decrease in leakage current at low temperature operation, recent analytical studies [7] have shown that the performance of a CMOS chip has the potential of achieving a 4.3X performance enhancement at –100°C for a power limited chip, as predicted by Equation 1 and shown in Figure 1.

$$f = \frac{T_{chip}}{358K}^{-\alpha} \qquad \text{for } \alpha = 0.5, 0.75, 2 \tag{1}$$

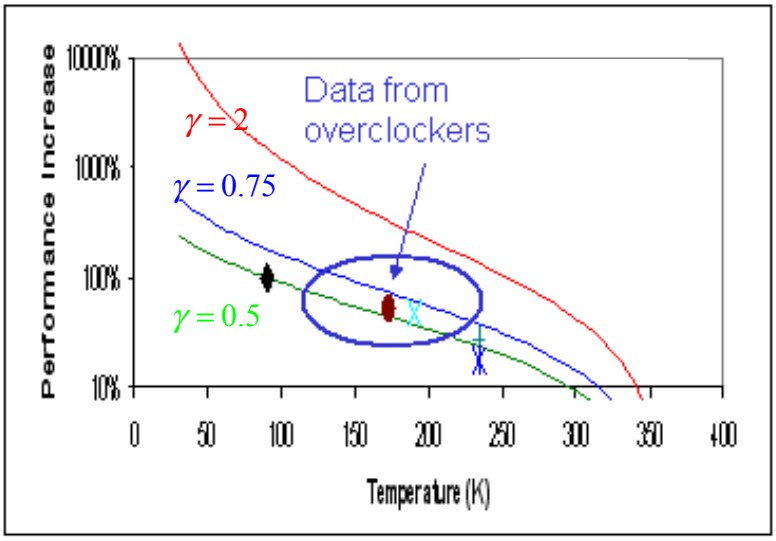

Figure 1: Chip performance scaling with temperature.

This enhancement can be explained by examination of Equation 2, which shows the total power as a sum of the leakage power and active power of the microprocessor.

$$P_e = N_{transistors} V_{dd} I_{leakage} + \frac{1}{2} a N_{tr} C_{ave} V_{dd}{}^2 f \qquad (2)$$

Because the leakage power decreases as the junction temperature is reduced, the frequency of a microprocessor may be increased for the same total power output

Despite these potential performance enhancements, there are some major drawbacks as chip temperatures are decreased to the cryogenic arena. For example, in order to maintain thermal insulation requirements for sub-ambient fluids flowing through tubing, expensive vacuum insulation pipe and bayonet valves must be used as cryogenic temperatures are approached, as opposed to rubber foam insulation at near ambient operation. Also, the cost of purchasing and operating a refrigeration/cryogenic system increases drastically as the operating temperature of the working fluid is lowered. Figure 2 illustrates this trend

by examining the current cost-performance scaling of various deep sub-ambient cooling technologies, as a function of evaporator saturation temperature. The data points shown in Figure 2 are initial and estimated operating costs that were obtained from Cryomech Inc. [2], Asetek Inc. [5], and Carrier Inc [6].

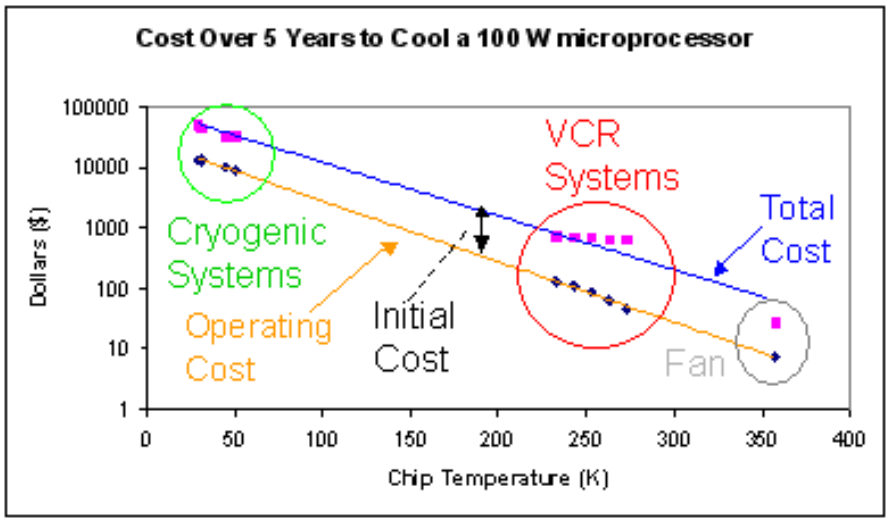

Figure 2: Cost-performance scaling of deep sub-ambient technologies with temperature.

Cryogenic technologies that can remove 100 W from a microprocessor at 100 K and below currently cost on the order of $20,000-$30,000 to purchase [2], have significant operational costs, and are quite large in size in comparison to their VCR counterparts. Such drawbacks would deter any desktop user from cooling their microprocessor to 100 K temperatures using a closed loop refrigeration cycle, despite the potential of large performance enhancements in computing power. When balancing the drawbacks and opportunities mentioned above, a cascaded VCR system was chosen as the most suitable technology for refrigeration of microprocessors. The cascaded VCR system was used as a test bed in the current study for the following reasons:

(1) Reliability – VCR systems can last more than 20 years with little or no maintenance required.

(2) Cost – VCR systems are two orders of magnitude cheaper than their cryogenic counterparts.

(3) Operating temperature – VCR systems can achieve –100 ^{o}C temperatures.

(4) Efficiency – Because vapor compression refrigeration is a mature technology, systems typically operate between 30-40% of a Carnot engine, as opposed to cryogenic systems that operate at less than 30% of Carnot efficiency. Also, the higher temperatures allow for a much higher coefficient of performance (COP), typically greater than 1 above –100 ^{o}C, as opposed to cryogenic systems with COP's on the order of 0.001.

1.2 Problem Statement and Tasks to Be Performed

Because vapor compression refrigeration is a mature technology, the current study does not aim at optimizing the refrigeration cycle, but rather interfacing the cascaded VCR system to the microprocessor via a compact evaporator capable of high heat flux and low temperature performance, with appropriate insulation requirements to avoid condensation or freezing of the electronics components.

The current study investigates four compact evaporator configurations at saturation temperatures between –86°C and –79°C, enabled by a cascaded R134a / R508b VCR system. The objectives of the current study are as follows:

- To determine the feasibility of interfacing a cascade vapor compression refrigeration (VCR) system to a desktop microprocessor.
- To characterize and recommend an ultra low temperature evaporator design that enables superior heat transfer performance at –79 to -86 ^{o}C.
- To perform flow visualization to help interpret the heat transfer and pressure drop results.
- To determine the accuracy of correlations available in the literature in predicting the heat transfer and pressure drop conditions in the current study.

LITERATURE REVIEW

In the past, a number of studies have addressed saturated flow boiling in single stage VCR macro-channel evaporators for servers and micro and mini-channel evaporators for microprocessors at near or above ambient conditions. Typically the hydraulic diameter is less than 1 mm for micro-channels, between 1-2 mm for mini-channels, and greater than 2 mm for macro-channels.

IBM conducted a packaging feasibility study of sub-ambient evaporators for a single stage VCR system [8] by removing 850-1050 W of dissipated power from 30 chips on their multi-chip module servers G4-G6 at sub-ambient temperatures between 15-35 ^{o}C. Even though the system was modular and of reasonable size, IBM had issues with condensation occurring on the electronic components and concluded that placing heaters alongside the evaporator was the best solution, despite reductions in heat removal capacity.

Many investigators [9-11] explored the design of micro-channel cooling devices using fluids with boiling points near or above ambient temperatures at ambient pressures. These investigators used water, fluorocarbons, and refrigerants such as R113 in single phase flows, and then used the latent heat of evaporation up to a vapor quality of 10% to obtain even higher heat fluxes at above ambient chip temperatures. The typical 85 ^{o}C temperature constraint for CMOS operation limits many of these two-phase cooling

methods, and fluids with low temperature boiling points become much more attractive because of their ability to achieve near critical heat flux (CHF) conditions.

Bowers and Mudawar [9] studied water in single and two-phase flows through copper evaporators. They recommended using a mini-channel over a micro-channel geometry because the pressure drop in their micro-channels (510 um) was 10 times greater than in the mini-channels (2.54 mm), while the heat transfer and critical heat flux performance were similar. Jiang [11] studied water in single and two-phase flows in 40 100x100 um channels. The study was limited to 9 ml/min because pressure drops approached 0.9 bar. The main contributor to the pressure drop in these studies was the accelerational pressure drop, which occurs due to the acceleration of liquid mass as it is converted to vapor along the channel. The accelerational pressure drop magnifies quickly at high vapor qualities and can become quite large as the cross-sectional area of the channels is reduced.

A summary of macro and micro channels evaporators for cooling of microelectronics is given in Table 1.

Table 1: Summary of macro- and micro-channel evaporators for cooling of microelectronics. $\dot{\forall}$ (volumetric flow rate), x_e (local quality), D_h (hydraulic diameter), W_{ch} (channel width), H_{ch} (channel height), L_{ch} (channel length).

Investigator	**Fluid** $\dot{\forall}$ **(ml/min) Subcooling (^{o}C) Local Quality x_e**	**Channels D_h, W_{ch}, H_{ch} L_{ch} Dimensions in mm**	**CHF on chip (W/cm^2) q" at 85 ^{o}C**	**Max ΔP (mbar)**	**Volume of Channels (mm^3)**
Bowers and Mudawar (1994)	R113, $\dot{\forall}$ = 64 20 ^{o}C - x_e=0.15	3 circular channels d_h = 2.54 17 channels d_h =0.51	CHF=256/ 200 q"=5	P_{drop} = 30/300 for d_h=2.54/ 0.51	435 / 88
Gillot (1999)	Water, $\dot{\forall}$ = 60 36 ^{o}C - x_e=0.12 FC72, $\dot{\forall}$ = 600 20 ^{o}C - x_e=0.2	6 circular channels d_h = 2	N/A Dimensions were not clear	N/A	N/A
Jiang (2002)	Water, $\dot{\forall}$ = 9 80 ^{o}C - x_e=0.1	40 rectangular channels W_{ch}=0.1 H_{ch}=0.1 L_{ch}=15	CHF N/A q"=14.2	900	6
Qu and Mudawar (2003)	Water x_e=0 – 0.15	21 rectangular channels W_{ch}=0.231 H_{ch}=0.712 L_{ch}=44.8	N/A Only presented correlation		155
Lee and Mudawar (2005)	R113 x_e=0.26-0.87	53 rectangular channels W_{ch}=0.231 H_{ch}=0.713 L_{ch}=25.3	N/A Only presented correlation		221

Even though two phase micro-channel heat sinks require a lower mass flow rate, have very large convective heat transfer coefficients, and have a uniform coolant temperature,

there are some practical challenges for implementing them in thermal management. Many authors [12-14] have reported bubble growth in micro-channel heat sinks resulting in severe pressure drop oscillations, vapor backflow, and premature critical heat flux conditions in the bubbly flow regime. In current study the inlet quality of the refrigeration fluid is greater than 0.35, and annular flow is the dominant flow regime. Flow reversals are usually circumvented in the annular flow regime due to the high superficial liquid and vapor velocities and the absence of bubbly flow. Under annular flow conditions, the high vapor velocity core can entrain the thin liquid film near the wall and cause a premature dry out on the channel wall, causing a sudden drop in the heat transfer coefficient [15].

INSTRUMENTATION AND EQUIPMENT

3.1 Evaporator Fabrication

The initial plan was to evaporate the refrigerant directly off the backside of the microprocessor, so silicon was chosen as the evaporator material. Evaporators were fabricated on silicon wafers by using the ICP process for 2000 cycles to create enhancement structures 1 mm deep in a 2 mm thick silicon wafer. However, the buna-n gasket that sealed the silicon evaporator became glassy at –50 ^{o}C and lost its sealing abilities, therefore PTFE (Teflon) had to be used as a gasket. Because a large compressive force is required to maintain an adequate seal with PTFE, the silicon evaporators shattered.

As a result of this setback, copper was chosen over silicon as a suitable evaporator material because of its durability, mechanical strength, and high thermal conductivity. A copper evaporator can be easily brazed and soldered to the copper tubing of the VCR system. The main drawback is that copper has a large coefficient of thermal expansion mismatch to silicon, and repeated thermal cycling between room temperature and –80 ^{o}C can fracture the microprocessor if the evaporator is soldered directly to the chip. Therefore, from a packaging perspective, thermal grease would be the preferred method of attachment, which generally has a much higher thermal resistance than a direct solder bond.

To avoid large temperature glides across the evaporator due to large accelerational pressure drops, it was desirable to choose flow boiling enhancement structures with the largest cross-sectional area possible, while maintaining structural integrity. At the same time, smaller cross-sectional areas and hydraulic diameters would allow for higher mass fluxes and thinner liquid films in the annular flow regime, yielding higher heat transfer coefficients. Perhaps even more important is an increase in the surface area available for heat transfer. Enhancement structures of various shapes were chosen to investigate the effect on evaporator performance.

The geometries considered were micro-channels, inline pin fins, alternating pin fins, and a baseline design with no microstructures for comparison purposes. The inline pin fin geometry was chosen in order to increase heat transfer by disrupting the boundary layers. The alternating pin fins were chosen to increase heat transfer at high heat fluxes (when dryout is expected) by catching the entrained droplets in the vapor core at each alternating row, and therefore re-wetting the surface for evaporator cooling. The pin fin geometries are expected to have a higher pressure drop than the micro-channels due to a breakup of the hydrodynamic boundary layer and increase in friction.

A 0.4 mm wide 1.2 mm deep end mill was used to mill four compact evaporators from a 3.1 mm thick by 20 mm long by 36 mm wide piece of copper. Each evaporator contains 2 manifolds that are 10 mm x 10 mm by 1.2 mm deep, and a 10 x 10 mm area to evaporate the refrigerant.

Table 2: Compact evaporators used in the current study.

Type of Evaporator	Description Dimensions in mm	Location in Figure 3
Baseline	Flat surface, no channels or pin fins. 10 wide by 1.2 deep	Bottom right
Micro-channel	13 channels, 0.4 deep by 1.2 deep, spacing of 0.8, d_h=0.6, A_c=6.24 mm^2	Bottom left
Inline Pin Fin	78 pin fins, 0.4 wide by 0.4 um long by 1.2 high, spacing of 0.8.	Top left
Alternating Pin Fin	84 pin fins, same dimension as inline pin fins but alternating	Top right

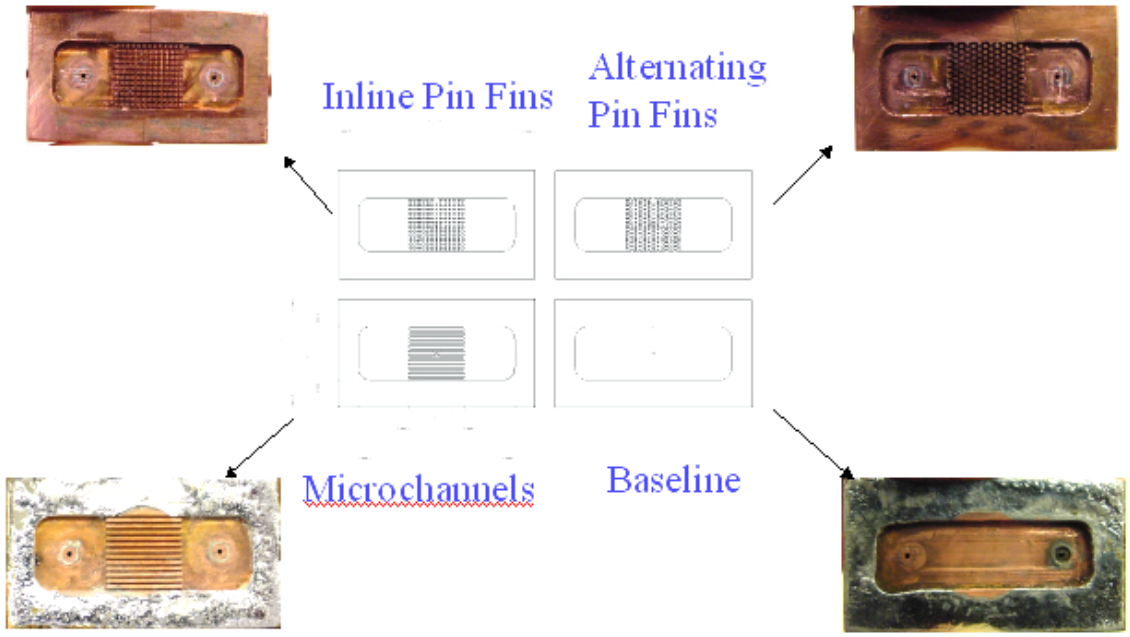

Figure 3: Top view of the microstructure evaporators.

3.2 Experimental Setup

3.2.1 Refrigeration flow loop

A two-stage cascade VCR system shown in Figure 4 is used to deliver R508b to the test module to characterize the four different evaporators shown in Figure 3. The evaporating R134a in the high temperature stage removes heat from the condensing R508b refrigerant in the low temperature stage. The two stages are capable of delivering R508b refrigerant to the test module at inlet pressures of 1-2.5 bar, flow rates of 50 to 70 g/min, and temperatures between –79 ^{o}C to –86 ^{o}C. An oil separator on the low stage was used to remove the polyolester oil (used to lubricate the compressor) from reaching the evaporator, where it can start to solidify at –80 ^{o}C temperatures. A filter/drier was placed on each stage of the refrigeration cycle to remove water moisture, acid build up, and any solid particles that could clog the micro-channels and micro pin fins. The amount of refrigerant charge and the adjustable flow coefficient of the needle valve determine the flow rate as well as the evaporator and condenser saturated pressures and temperatures. Shutoff valves were placed before and after the test module so that it could be detached and the different evaporator test structures could be exchanged. An accumulator with heaters was placed after the test module and before the flow meter so that any unevaporated refrigerant could be boiled off when the heat load on the evaporator was below the cooling capacity of the VCR system. Because the mass flow meter is designed to measure only single-phase liquid or vapor, the mass flow meter was placed after the accumulator were only superheated vapor is present. The heat load in the accumulator was adjusted so that the superheated vapor before the mass flow meter was above 0 ^{o}C so that the buna-n o-rings inside the flow meter could maintain their sealing properties.

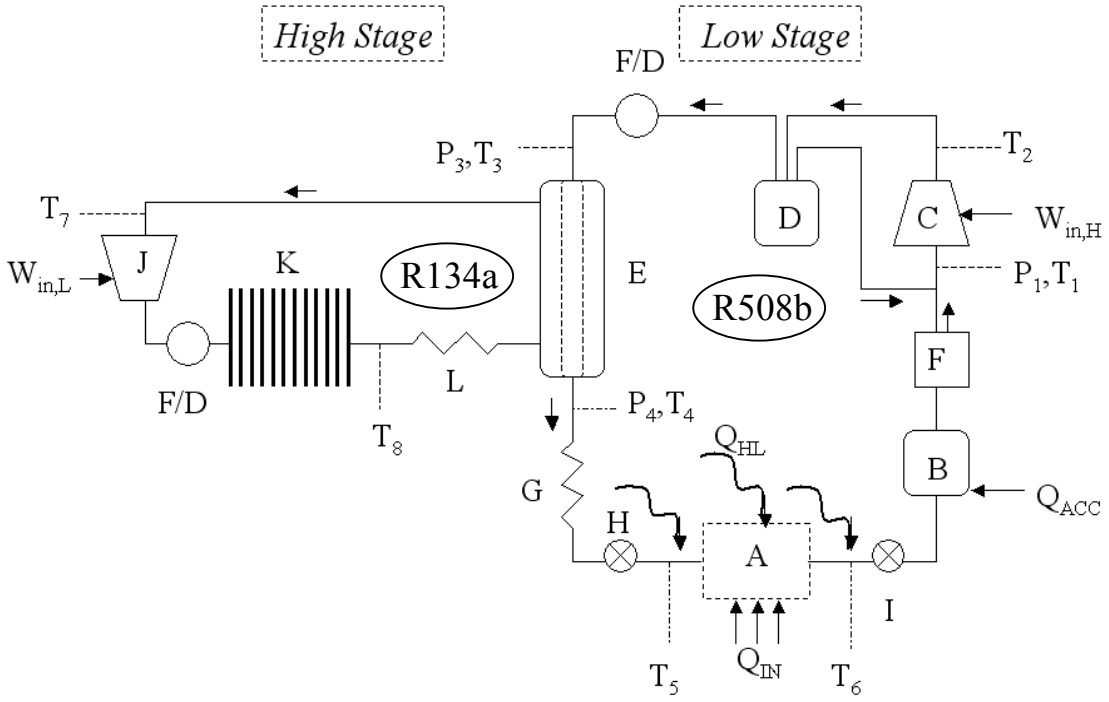

A – Test Module
B – Accumulator
C – ½ HP Low Stage Compressor
D – Low Stage Oil Separator
E – Heat Exchanger
F - Flow meter
G – Needle Valve
H, I - Shutoff Valves
L – Capillary Tube
J - High Stage Compressor (1/2 HP)
K - Air Cooled Condenser
F/D – Filter Drier

Figure 4: Schematic of the cascade refrigeration system.

3.2.2 Test module

The test module was used as a test bed for determining the pressure drop and heat transfer characteristics of the four evaporator design candidates and is shown in Figure 5 and Figure 6. The test module was also designed to enable optical access for visualization of the R508b refrigerant evaporating inside each evaporator.

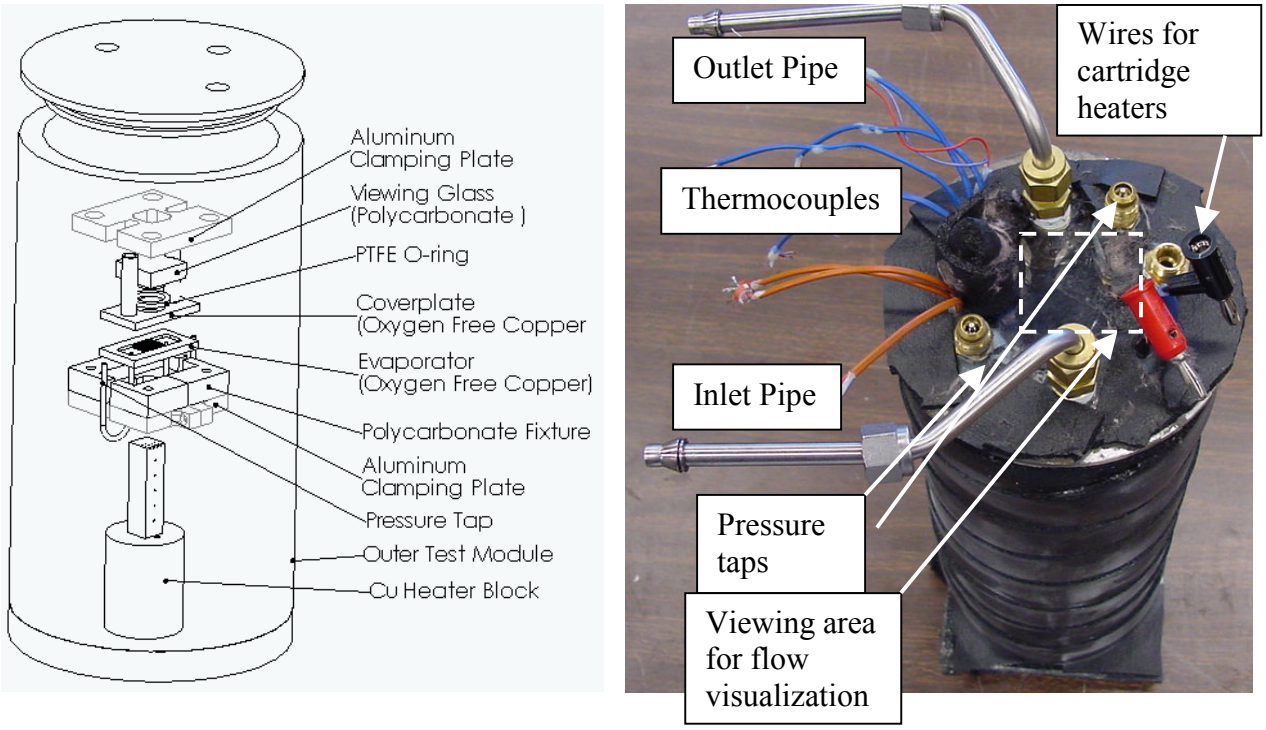

Figure 5: Inner and outer test module

The outer test module comprises of a 4-inch diameter 12-inch high polycarbonate cylinder, and a polycarbonate cover plate that seals the cylinder via a Buna-n o-ring. It is used to insulate the inner module from the ambient by drawing a 100-mbar vacuum around the inner module and aids in flow visualization by evacuating any water moisture that could condense or solidify on the inner cover plate. The inlet and outlet pipes, thermocouples, electrical wire for the heater, and pressure taps are run through the cover plate and sealed using a 4-hour cure time Loctite epoxy.

The inner test module is shown in detail in Figure 6 and comprises of a viewing window, a copper cover plate, an evaporator test sample, pressure taps, and a copper heater block.

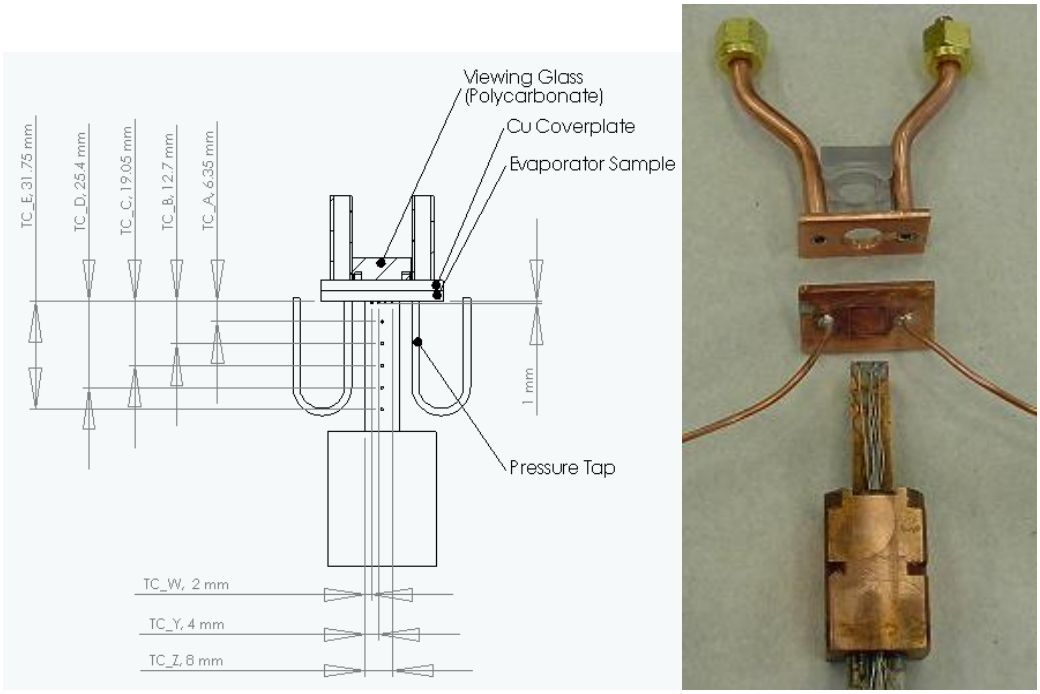

Figure 6: Side view of inner test module before assembly.

The heater block was used to simulate a microprocessor by providing a uniform heat flux up to 200 W/cm^2 over 1 square cm contact area to the back of the evaporator samples, just underneath the micro-structures. The copper heater block contains two 100 W Omega cartridge heaters attached thermally to the copper block using Arctic Ceramique thermal grease, made by Arctic Silver, Inc. An AC transformer made by Staco, Inc. was used to control the supply voltage for the heaters and a precision resistor (0.2 ohm +/- 1%) was connected in series with the cartridge heaters to determine the supply current. Eight 0.51 mm T-type Omega thermocouple probes were inserted into the full length of the eight 1 mm diameter holes shown in Figure 6 and epoxied at the surface using a 4-hr cure time Loctite epoxy. Three thermocouples (W,Y,Z) place at 2 mm, 6 mm, and 8 mm along the flow direction and 1 mm below the heater block surface were used to report local surface temperatures of the heater block. The remaining five evenly spaced

thermocouples were inserted along the length of the heater block to confirm a 1-D temperature gradient in the heater block. Pressure taps were constructed by soldering two capillary tubes (0.034" inner diameter) to the bottom of the evaporator manifolds.

Sn62 Indium solder (0.002" thick) and Indium 5RMA flux were used to solder the cover plate and the heater block to the evaporator sample. Pictures were taken during and after the soldering process to illustrate the assembly, as is shown in Figure 7. The left picture shows the Sn62 solder ribbon before the soldering process. The center picture shows the soldering of the copper cover plate to the evaporator sample. The right picture shows the solder on the heater block surface after it was removed from the evaporator and testing was completed. The uniformity of solder on the surface confirms that the thermal connection between the heater block and sample was reliable.

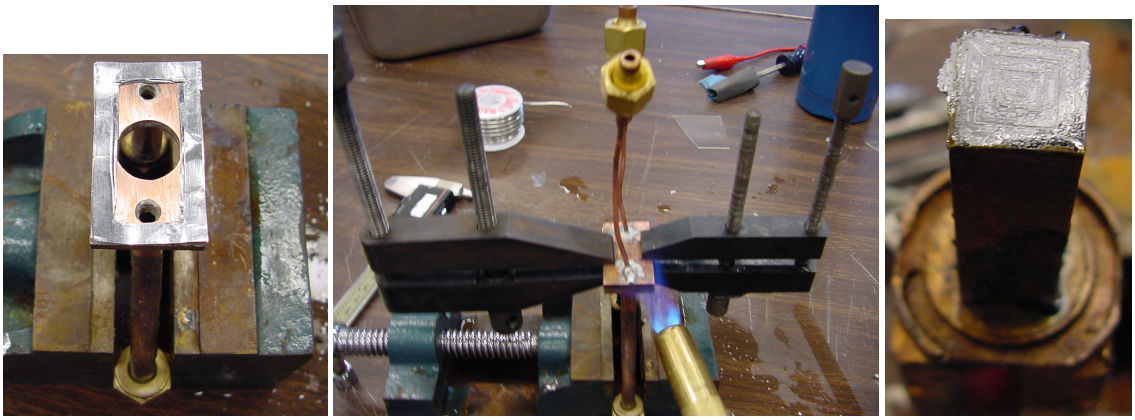

Figure 7: Soldering the copper coverplate and heater block to the evaporator sample.

The cover plate has a 12 mm diameter circular window removed, so that the boiling refrigerant may be visualized using a high-speed camera via a polycarbonate viewing glass. Visual observation confirmed that the polycarbonate and copper cover plate were flush, as shown in Figure 8. Assuming that the copper cover plate is flush with the

evaporator sample, the gap between the polycarbonate viewing glass and the enhancement structures is estimated to be no more than 0.005", ensuring that the majority of refrigerant would flow through, and not over, the enhancement structures.

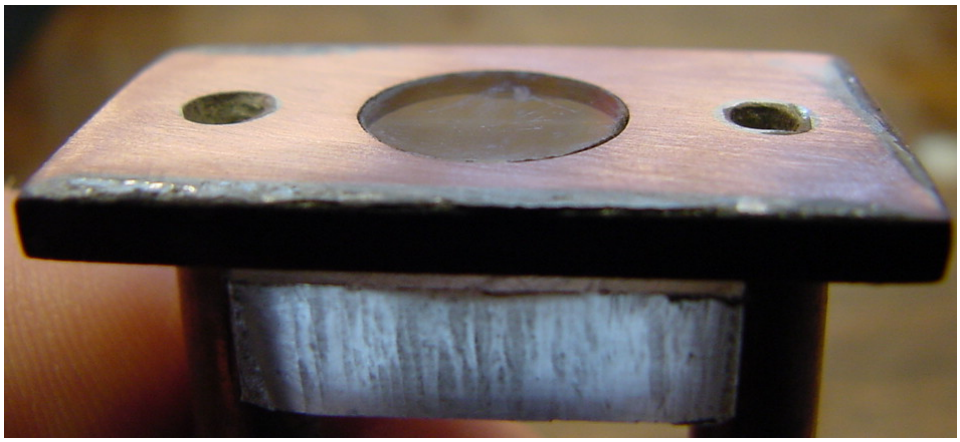

Figure 8: Backside of polycarbonate and copper cover plate.

A top view of the final assembly is shown in Figure 9. A PTFE o-ring between the copper cover plate and polycarbonate viewing glass prevents refrigerant from escaping the flow loop.

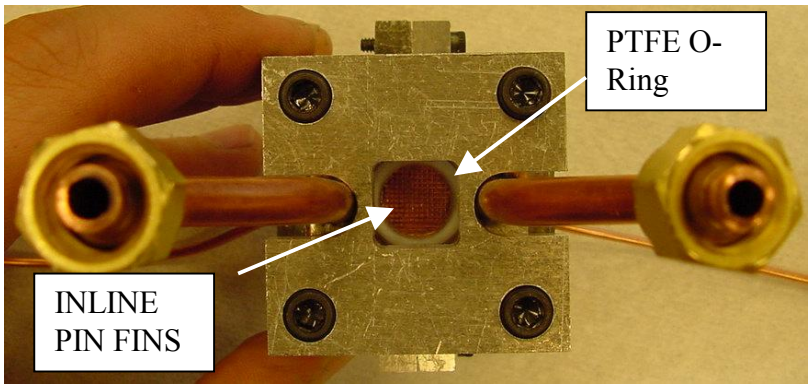

Figure 9: Top view of inner test module after assembly.

PTFE was the only known gasket and o-ring material that could provide a reliable seal at –80 ^{o}C temperatures, however because it deformed permanently after compression the o-

ring could not be re-used. Materials such as viton, buna-n, neoprene, and silicon become glassy as –50 to –60 ^{o}C temperatures were approached and lost their sealing abilities.

The full set of layout drawings used to construct all the required parts of the inner and outer test module are shown in Appendix A.

3.2.3 Experimental uncertainties

Uncertainties associated with the mass flow measurements were estimated to be less than 0.1 g/min. The heat flux entering the evaporator from the heater block was measured with an uncertainty of less than 1%. Uncertainty in the absolute pressure measurements were less than 1 mbar for heat fluxes less than 70 W/cm^2 and less than 2 mbar for higher heat fluxes. Uncertainties in the pressure drop were less than 3 mbar for all heat fluxes, and less than 1.5 mbar at heat fluxes less than 70 W/cm^2. Temperature readings on the system level (T_1-T_6) had uncertainties less than 1 ^{o}C. Thermocouples inside the test module that were used to calculate chip surface temperatures were estimated to have uncertainties of 0.5 ^{o}C, mainly due to the uncertainty of contact between the probe and heater block.

3.3 Test Procedure

After the evaporator sample was installed in the test module and connected to the low stage of the refrigeration system, the shutoff valves were opened and the pressure was allowed to equalize. While the compressors remained off, the low stage was charged with R508b refrigerant until it reached a static pressure of 8.5 bar. Because R508b is non-

saturated (fully vapor) at ambient temperatures, pressure is an effective means to gauge the proper charge of refrigerant. Before experiments were conducted, 25 minutes were required to achieve steady state conditions inside the evaporator. Approximately 10 minutes after the high stage compressor was turned on, the heat exchanger between stages achieved a temperature of –35 ^{o}C. Then, the 2nd stage compressor was turned on and required an additional 15 minutes to cool down the evaporator to –80 ^{o}C.

To obtain the required data, the flow rate was adjusted between 50 and 70 g/min and the heat flux was increased in increments of 10 W/cm^2 from 20 to 100 W/cm^2. During a given test, the flow rate was controlled to +/-0.2 g/min from the desired flow rate by opening or closing the needle valve. Once the flow rate stabilized, the power supply was adjusted by using a VAC Variac (0-120 V). The flow rate, pressure, temperature, and power values were monitored and recorded using an Agilent 34970A data acquisition system interfaced to a Dell computer. Steady state conditions were considered to be achieved once all eight thermocouple readings in the heater block changed no more than 0.3 ^{o}C over 1 minute. After achieving steady state, data was acquired every 3 seconds over a period of 3 minutes. At the same time, a high-speed Phantom V4.0 camera (1000 frames per second) was used to visualize the flow detail of the evaporating R508b in the compact evaporators.

3.4 Data Reduction

Once the data was obtained, the heat flux, heat transfer, pressure drop, saturation temperature, inlet and outlet qualities, heat leak, and the mean absolute errors (MAE%)

were determined using the following equations. The heat flux delivered to the evaporator is calculated by knowledge of the supply voltage and current to the cartridge heaters.

$$q''_{chip} = \frac{Q_{in}}{A_{chip}} = \frac{V_{in} I_{in}}{A_{chip}} \tag{3}$$

Because the supply was from an alternating current (AC) source, the root mean square (RMS) values for voltage and current were used in Equation 3. The average saturation temperature in the evaporator is calculated from the inlet and outlet saturation temperatures that correspond to the inlet and outlet saturated pressures.

$$T_{av,sat} = \frac{T_{i,sat} + T_{o,sat}}{2} \tag{4}$$

The local heat transfer coefficient between the wall and the refrigerant for the micro-channel geometry is calculated using equations 5 through 8 and is illustrated in Figure 10. Assuming insulated boundary conditions at the top of the channels, insulated boundary conditions on the side due to symmetry, and a uniform heat flux from the bottom of the evaporator base, these equations are used to model the heat transfer in the unit cell shown in Figure 10. These equations represent a resistor network that considers 1-D conduction through the copper evaporator base and a fin analysis on the channel walls.

$$q''\left(W_{ch} + 2W_w\right) = h_{tp}\left(T_{w,b} - T_{sat}\right)\left(W_{ch} + 2\eta H_{ch}\right) \tag{5}$$

$$\eta = \frac{\tanh\left(mH_{ch}\right)}{mH_{ch}} \tag{6}$$

$$m = \sqrt{\frac{h_{tp}}{k_s W_w}} \tag{7}$$

$$T_{w,b} = T_m - \frac{q'' H_{tc}}{k_s} \tag{8}$$

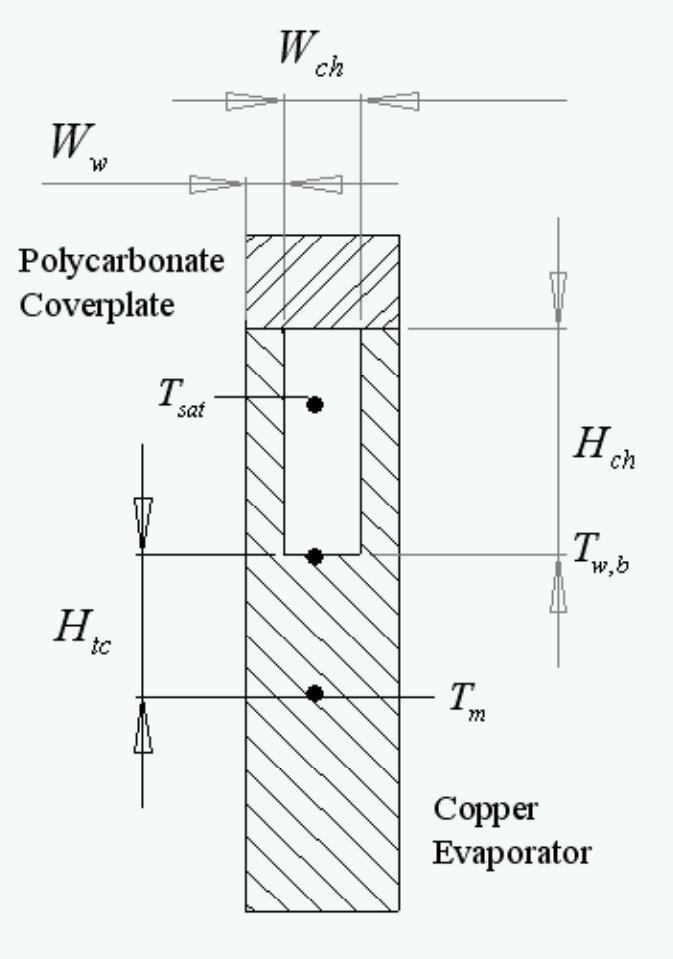

Figure 10: Cross-section of micro-channel evaporator.

The maximum chip temperature refers to the maximum temperature of the three thermocouple measurements installed along the flow direction:

$$T_{chip,\max} = \max\left(T_{m,W} + T_{m,Y} + T_{m,Z}\right) \tag{9}$$

The effective heat transfer coefficient and pressure drop inside the evaporator are given as:

$$h_{eff} = \frac{q''_{chip}\left(A_{chip} / A_w\right)}{T_{\max,chip} - T_{sat}} = \frac{q''_w}{T_{\max,chip} - T_{sat}} \tag{10}$$

$$P_{drop} = P_i - P_o \tag{11}$$

It is useful to calculate the inlet and outlet quality of the evaporator for flow visualization purposes and cooling capacity predictions. Knowledge of the temperature T_4 and pressure P_4 gives the enthalpy H_4 of the sub-cooled liquid before the metering valve. Assuming an isenthalpic drop in pressure at the metering valve, the inlet enthalpy H_i before the evaporator, provided there is no heat leak. Knowledge of the inlet pressure P_i and enthalpy H_i also gives the inlet quality x_i into the evaporator. The outlet enthalpy can be determined from an energy balance:

$$H_o = \frac{Q_{IN}}{\dot{m}} + H_i \tag{12}$$

By knowledge of the outlet pressure p_o and enthalpy H_o then outlet quality x_o can be determined. Because the heat flux is uniform spatially, the local quality is assumed to vary linearly from inlet to exit.

$$x(z) = \frac{(x_o - x_i)}{L} + x_i \tag{13}$$

In equation 13, L is the length of the enhancement structures in the flow direction, and is 10 mm long.

Because the evaporator reaches saturation temperatures between –86 ^{o}C and –79 ^{o}C, radiation, convection, and conduction allow heat from the ambient to leak into the evaporator. When the input power into the heat block, Q_{in}, exceeds the cooling capacity of the VCR system, $\left[Q_{in} > \dot{m}\left(H_{sat,vapor} - H_i \right) \right]$, the refrigerant is superheated at the exit

and the exit enthalpy H_o can then be determined. Only under these conditions can an energy balance be used to determine the heat leak, as shown in equation 14.

$$Q_{HL} = \dot{m}(H_6 - H_4) - Q_{IN} \tag{14}$$

where H_6 and H_4 are determined from the superheated vapor ($P_{6,}T_6$) after the evaporator and the sub cooled liquid ($P_{4,}T_4$) before the throttling valve, respectively.

The mean absolute error (MAE%) is used to assess the accuracy of correlations in predicting the heat transfer coefficients and pressure drop, and is defined as:

$$MAE\% = \frac{1}{N_{data}}\left[\sum \frac{h_{pred} - h_m}{h_m} \times 100\right] \text{ for heat transfer and} \tag{15}$$

$$MAE\% = \frac{1}{N_{data}}\left[\sum \frac{\Delta P_{pred} - \Delta P_m}{\Delta P_m} \times 100\right] \text{ for pressure drop.} \tag{16}$$

where $h_{pred}, h_m, \Delta P_{pred}, \Delta P_m$ are the predicted and measured heat transfer coefficients and pressure drops respectively.

3.5 Experimental Challenges

Despite various attempts at insulating the test module from the ambient, the heat leak into the evaporator was calculated to be between 20-32 W for all test runs from an energy balance between states 1 and 4. Aluminum foil was used on the inner walls of the outer test module to minimize radiation losses, and a 100 mbar vacuum was pulled in the outer test module to minimize natural convection around the evaporator. Unfortunately, the cover plate on the outer module could not be insulated since it provided visual access to the evaporator for flow visualization. It was concluded that this was the main pathway for

heat leak into the evaporator because ice build up was observed on the cover plate. The ice build up on the cover plate is shown in Figure 11.

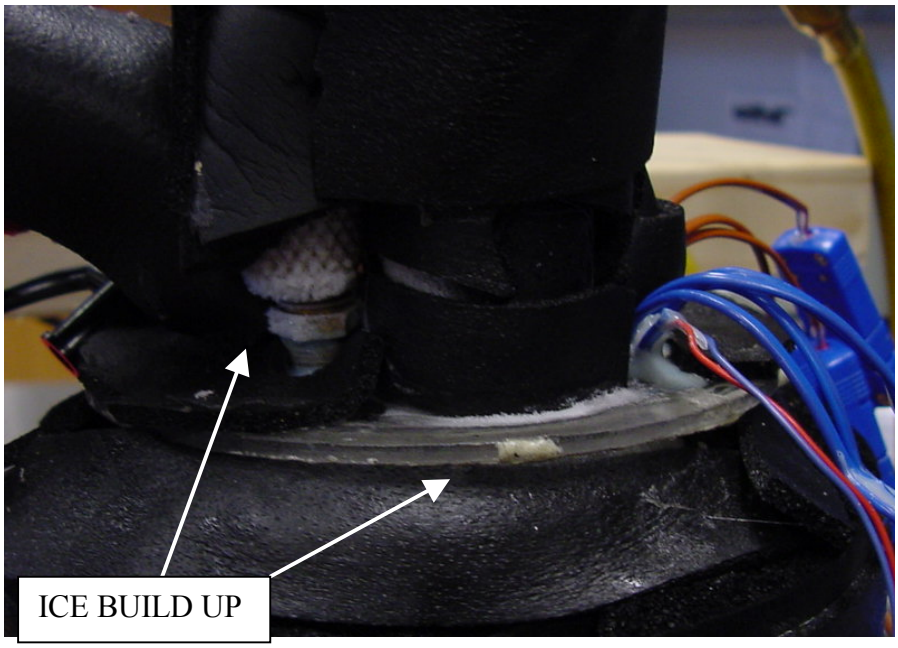

Figure 11: Ice build up on outer cover plate.

Ice build up on the outer cover plate prevented visual access to the flow boiling inside the evaporators. The outer test module cover plate was made out of transparent polycarbonate to obtain optical access to the test structure. Even though the viewing glass in the inner test module was fully transparent, water moisture from the atmosphere condensed and froze on the outer cover plate, impairing the camera's vision. This was mainly because the inlet and outlet pipes containing refrigerant at –80 ^{o}C and fed through the cover plate to the evaporator were placed too close to the viewing area of the camera. Placing insulation over the outer test module cover plate was not an option because it would block optical access to the evaporator. Placing transparent heaters on the cover plate was deemed unacceptable because it would increase heat leak into the evaporator.

A second generation outer test module was constructed for flow visualization experiments. It allows for vacuums less than 1 mbar and provides access for flow visualization by moving the inlet/outlet pipes away from the camera's viewing area. This outer test module is explained further in the flow visualization section of the results and discussion chapter.

RESULTS AND DISCUSSION

Experiments were performed to determine the local and maximum chip temperatures for the various evaporator designs for $\dot{m}$=50-70 g/min and q"=20-100 W/cm^2. The evaporator that provides the lowest chip temperatures for the range of heat fluxes considered will be the recommended design. The chip temperature is dependent on the heat transfer and pressure drop characteristics of the evaporator, which determine the saturation temperature T_{sat} and chip superheat (T_{chip}-T_{sat}) respectively. Therefore, the heat transfer and pressure drop characteristics will be used to interpret the results.

4.1 Pressure Drop and Saturation Temperature

There are two factors that determine the average saturation temperature of the evaporator T_{sat}: the pressure drop across the evaporator and the dynamics of the refrigeration system external to the evaporator. Large pressure drops can cause a saturation temperature glide across the evaporator that can significantly increase the chip temperature, especially at low flow rates. For example, a pressure drop of 1 bar across the evaporator will cause the saturation temperature to glide 13 ^{o}C. Unlike single-phase system pumps, compressors on a two-phase VCR system can accommodate large pressure drops in the evaporator because they can supply pressure heads of up to 20 bar. However, much of that pressure drop should be incurred in the expansion device to supply low temperatures to the evaporator. The pressure drops across the micro-features of the evaporator, ΔP_m, are shown in Figure 12. The top left graph shows the effect of flow rate on the pressure drop

for the baseline evaporator. The remaining three graphs show the effect of evaporator geometry at fixed flow rates of 50 g/min (top-right), 60 g/min (bottom-left), and 70 g/min (bottom-right).

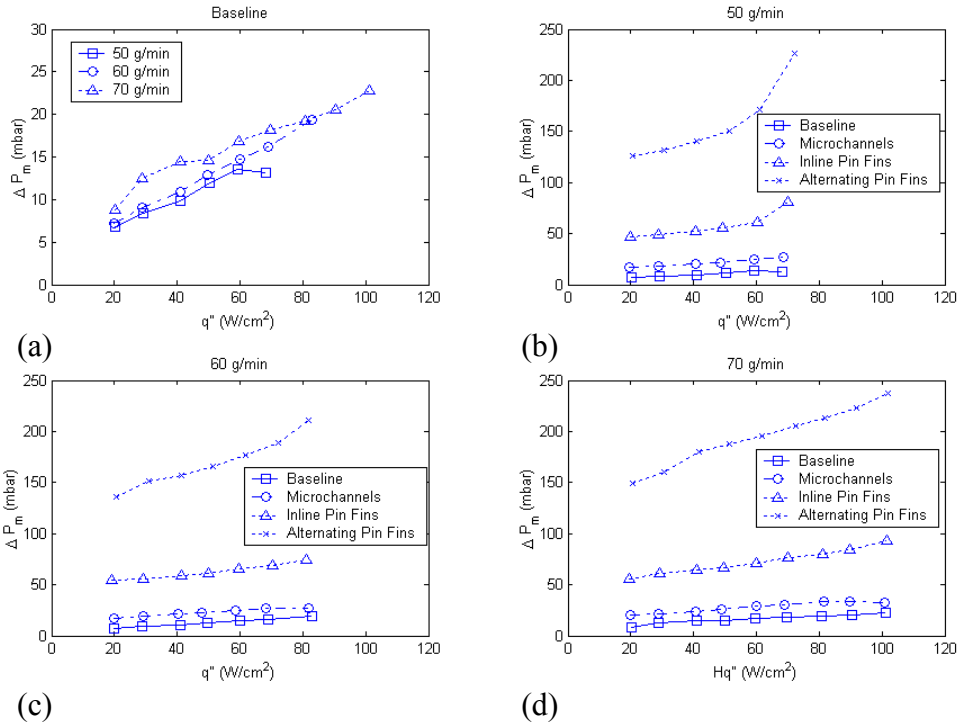

Figure 12: (a) Effect of flow rate on pressure drop in the baseline evaporator. Effect of geometry on pressure drop at (b) 50 g/min, (c) 60 g/min, (d) 70 g/min.

The dynamics of the refrigeration system are also important in determining the saturation temperature. When the needle valve is opened, the flow rate is increased, and the condenser and evaporator saturation pressures/temperatures are increased due to an increase of vapor and decrease of liquid in the system. Figure 13 shows the saturation temperatures of the baseline evaporator under various flow rates. The average saturation temperature increases with increasing heat flux and flow rate. This can be explained by examining the average saturation pressure. As the flow rate or heat flux is increased the pressure drop increases, raising the average saturation pressure for a fixed exit saturation

pressure. As a result, the average saturation temperature is also increased because pressure and temperature are directly related in the saturated regime.

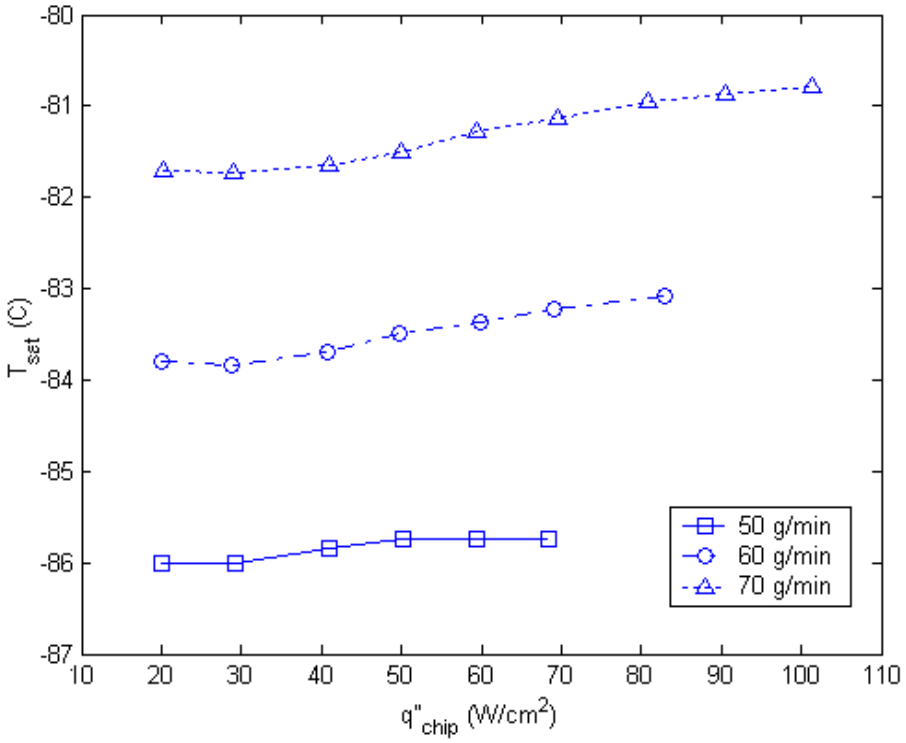

Figure 13: Saturation temperature vs. heat flux for three different flow rates.

4.2 Chip Temperatures and Heat Transfer

Figure 14 (a) shows the convective boiling curves associated with three different flow rates in the baseline structure. The remaining three graphs in Figure 14 compare the boiling curves of all four evaporator structures at flow rates of 50, 60, and 70 g/min. These boiling curves are conservative measures of performance because only the heat flux inputted by the cartridge heaters was reported, neglecting the 20-32 W of heat leak.

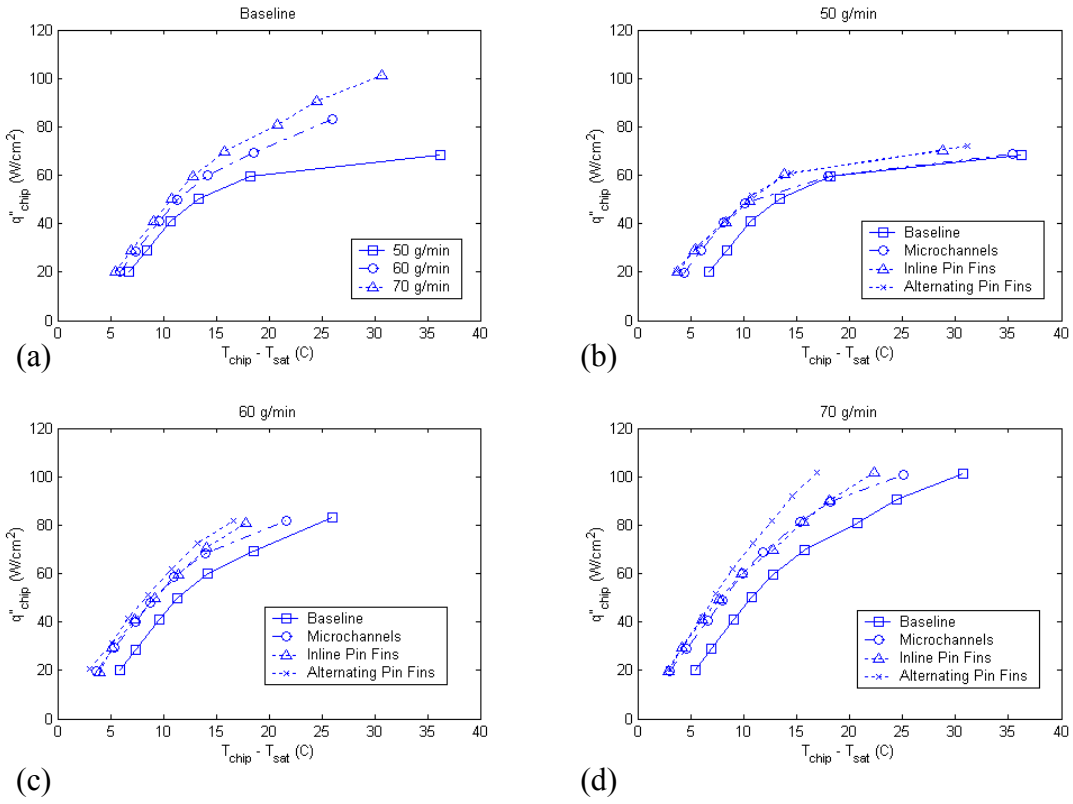

Figure 14: (a) Effect of flow rate on the boiling curves for the baseline geometry. Effect of geometry on the boiling curves for (b) 50 g/min, (c) 60 g/min, (d) and 70 g/min.

The following observations are readily apparent from the graphs.

- The flow rate has a large effect on the heat transfer, which indicates that convective heat transfer, and not nucleate boiling, is the dominant heat transfer mechanism.
- In order to keep chip superheats low under high heat flux conditions, larger flow rates are necessary to avoid dry out conditions.
- The chip superheat can be reduced either by increasing the mass flow rate through each of the evaporators or introducing micro-channels or micro pin fins into the baseline evaporator.

- The chip superheat increased dramatically once a specific heat flux was achieved, indicating a detachment of the liquid film from the enhancement structures (dry out), however dry out conditions could not be confirmed visually. Heat transfer degradation occurred at higher heat fluxes for high mass flow rates.
- The alternating pin fins had the lowest chip superheats of all four evaporators, especially at high flow rates and high heat fluxes.

The effective heat transfer coefficients h_{eff} vs. exit vapor quality x_o are shown in Figure 15.

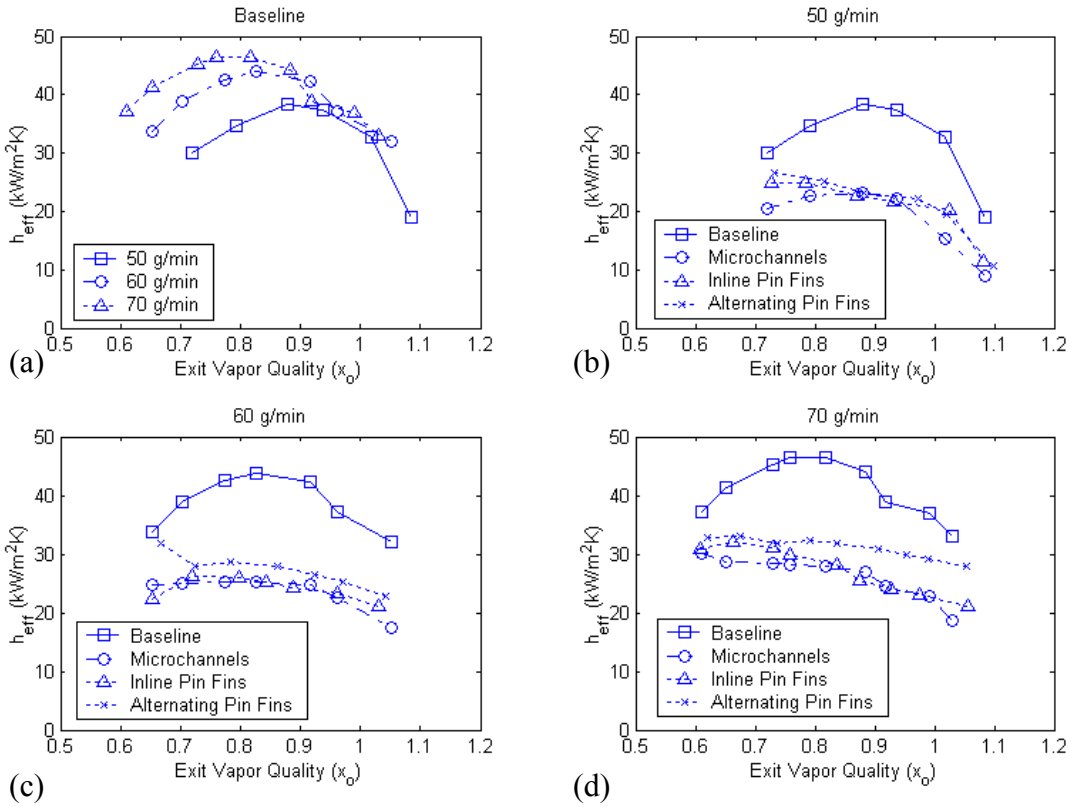

Figure 15: (a) Effect of flow rate on the effective heat transfer coefficient for the baseline geometry. Effect of geometry on the effective heat transfer coefficient for (b) 50 g/min, (c) 60 g/min, (d) 70 g/min.

Because the heat leak was calculated to be 20-32 W when the flow was superheated at the exit, the exit vapor quality was estimated by assuming a heat leak of 30 W and using equation 17 to obtain the exit enthalpy:

$$H_o = \frac{Q_{IN} + Q_{HL}}{\dot{m}} + H_i \tag{17}$$

The heat transfer coefficient was plotted versus the predicted exit quality to determine whether dry out was due to complete vaporization of the refrigerant or due to detachment of the thin liquid film on the wall. It was concluded that the liquid film was detached from the wall before the exit of the enhancement structures because their was a gradual

decrease in heat transfer coefficient before an exit quality of 1. The effective heat transfer of the baseline evaporator increased with exit vapor quality up until 80%-90% depending on flow rate, and then decreased as dry out occurred near the exit of the evaporator. For the other structures, the heat transfer coefficient seems to be constant and then drop at high qualities.

Comparison of Figure 14 and Figure 15 shows that the reduction in chip superheat for the micro-channel and inline/alternating pin fins was due to an area enhancement and not in improvement in their effective heat transfer coefficients.

Figure 16 shows the maximum chip temperature for a given heat flux. For heat fluxes lower than 60 W/cm^2, the saturation temperature plays a large role in determining the maximum chip temperature because chip superheats are small. In this case a lower flow rate is recommended to maintain low chip temperatures. However at heat fluxes above 60 W/cm^2, the chip temperature was best maintained by pumping high flow rates through the alternating pin fin geometry. For example, at 100 W/cm^2, the lowest chip temperature of –62.6 ^oC was obtained by using the alternating pin fin evaporator at 70 g/min.

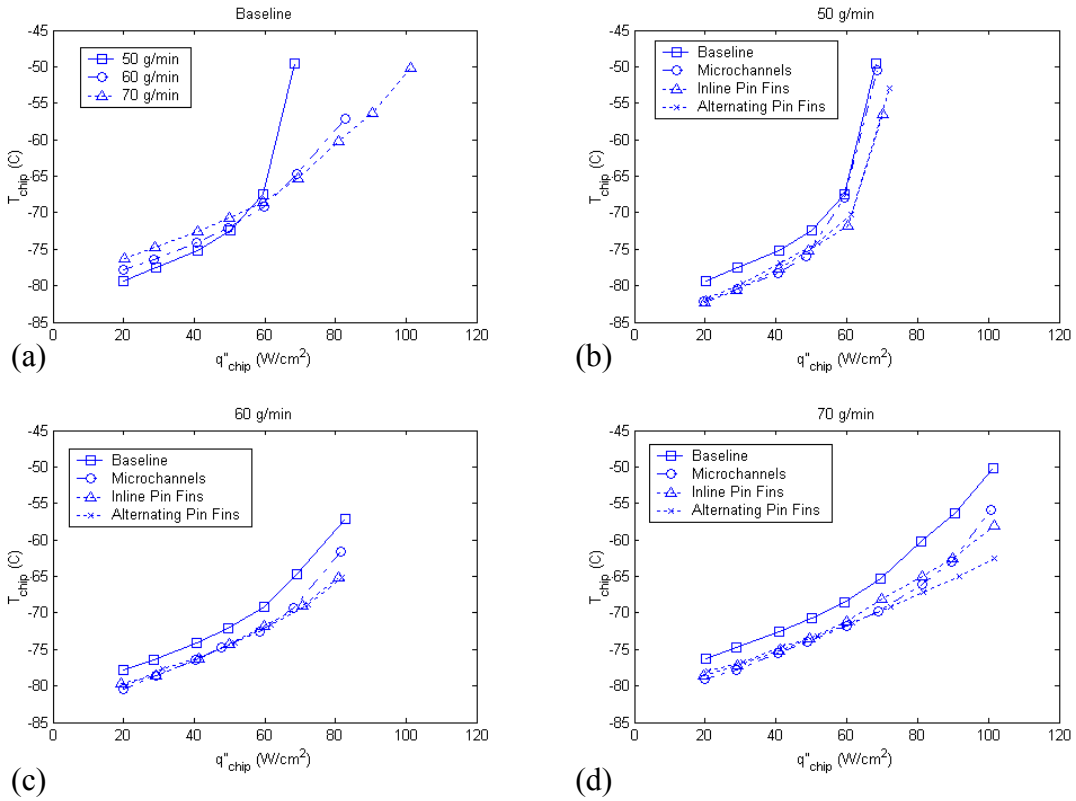

Figure 16: (a) Effect of flow rate on the maximum chip temperature for the baseline geometry. Effect of geometry on the maximum chip temperature for (b) 50 g/min, (c) 60 g/min, (d) 70 g/min.

For a flow rate of 50 g/min, chip temperatures increased almost 20 ^{o}C in every evaporator geometry as the heat flux was increased from 60 to 70 W/cm^2 due to a sudden dry out condition along the channel walls. For the micro-channel geometry flow visualization confirmed this observation, as is shown in Figure 21. This will be discussed in greater detail in section 4.3.

Chip temperature uniformity was investigated because the presence of large temperature gradients inside the silicon can create local stresses, potentially reducing the lifespan of the microprocessor. Fortunately, the decrease in saturation temperature and heat transfer

coefficient across the evaporator can counteract each other to produce uniform chip temperatures. Figure 17 shows the measured chip temperatures at three steam-wise locations from the entrance – 2 mm ($T_{m,W}$), 6 mm ($T_{m,Y}$), and 8 mm ($T_{m,Z}$), as shown in Figure 6. For heat fluxes less than 40 W/cm^2, chip temperature variations are smaller than the uncertainties of the temperature readings. The largest variation in local chip temperatures occurred at high heat flux, low flow rate conditions where exit vapor qualities larger than 90% are encountered. The baseline geometry had the largest temperature variation of 2.5 ^{o}C at 50 g/min and 70 W/cm^2. Temperature variations of this magnitude present no threat in reducing the lifespan of the microprocessor.

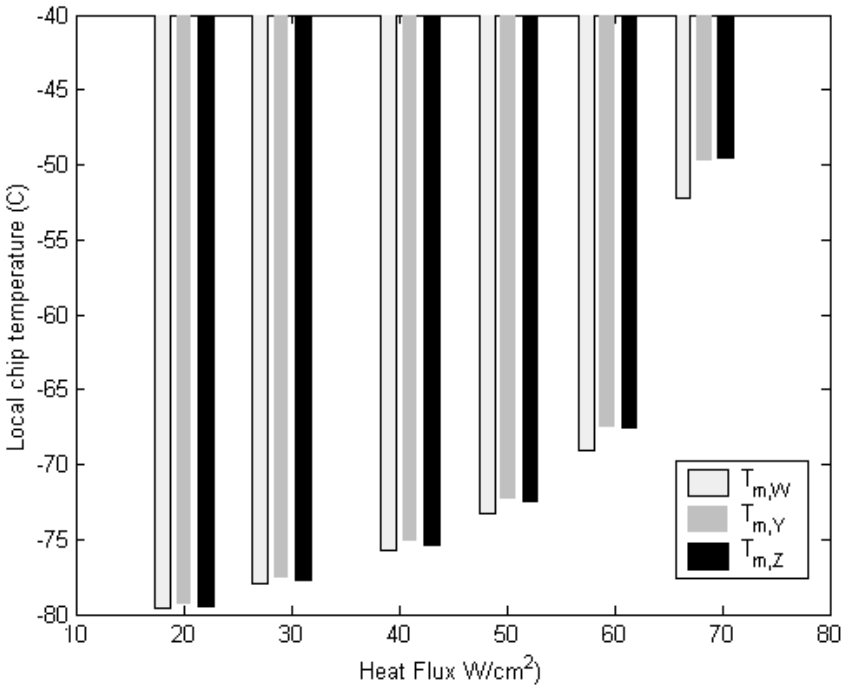

Figure 17: Local chip temperature vs. heat fluxes for the baseline geometry at 50 g/min.

4.3 Flow Visualization in Micro-channels

Flow visualization was not possible in the first generation test module because of ice build up on the polycarbonate cover plate, as shown in Figure 11. A re-design of the outer test module was required to improve optical access into the evaporator. The following improvements were made, resulting in the 2nd generation outer test module shown in Figure 18.

- Stainless steel was chosen as the outer module material instead of polycarbonate because it can be welded for sealing purposes, has a relatively low conductivity in comparison to other metals (k_s < 15 W/mK), and has a high resistance to corrosion.
- The inlet and outlet pipes were moved away from the polycarbonate viewing area.
- Compression tubes fittings and welded stainless steel connections replaced epoxy connections as sealing methods when feeding thermocouples, heater wires, and piping through the cover plate.

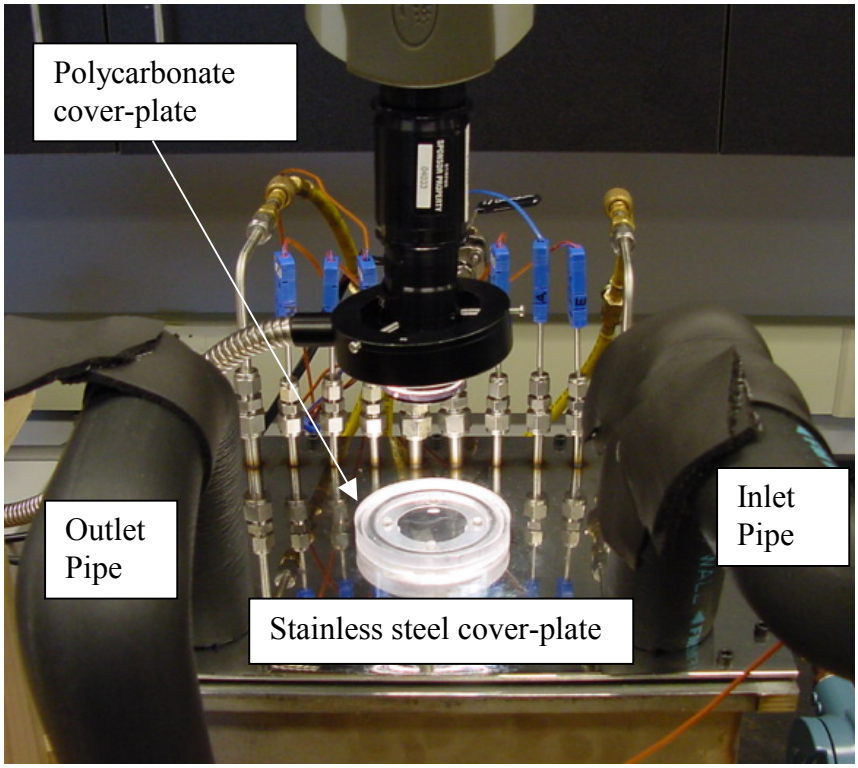

Figure 18: Picture of 2nd generation outer test module.

As a result of these design modifications, the outer test module was able to retain vacuums of 0.5 mbar (0.38 torr), resulting in negligible icing of the polycarbonate viewing glass (see Figure 5 for assembly with polycarbonate viewing glass). Because there was approximately four inches of distance between the polycarbonate cover plate and the inlet/outlet pipes, the polycarbonate cover plate was at ambient temperatures and no condensation or freezing of air moisture occurred on its surface. Despite these improvements, camera visibility was limited by the small micro-channel size, lighting requirements, and internal reflection within the micro-channel.

Tests were conducted for the baseline geometry at a flow rate of 50 g/min and heat fluxes of 20-70 W/cm^2. Unfortunately, there was no reduction of heat leak into the test module, as all thermocouples reported similar results that were obtained with the first generation

outer test module. A Phantom V4.0 camera captured the evaporating refrigerant. An exposure time of 1.98 ms was chosen because it allowed enough light into the camera so that the image was of decent quality, however this limited the cameras maximum frame rate to 500 frames per second (fps).

In order to understand what set of images the camera will capture it is useful to predict the distance traced by liquid and vapor particles between consecutive frames, Δz_{frame}. Predictions were obtained by calculating the vapor and liquid velocities from the separated flow model [15], as shown in Equations 18 - 20 below.

$$\Delta z_{frame} = u\left(\frac{1}{500\,\mathrm{sec}^{-1}}\right) \tag{18}$$

$$u_f = \frac{G}{\rho_f \alpha} \tag{19}$$

$$u_g = \frac{G}{\rho_g (1-\alpha)} \tag{20}$$

Figure 19 shows that at 500 fps, the Phantom camera will capture a video frame of a liquid particle every 1-2 mm and a vapor particle every 7-17 mm, depending upon position inside the channel.

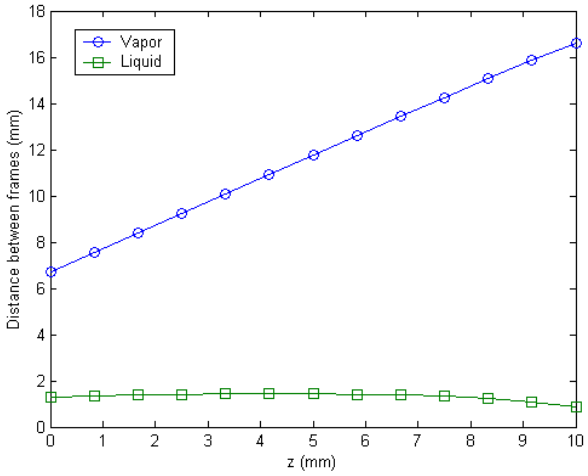

Figure 19: Predicted Δz_{frame} at 50 fps, 50 g/min, and x_e=0.35-0.95.

Figure 20 (a) is a video of a top-view of the channels at 50 g/min and zero input power. The video shown in Figure 20 (b) is the same capture but uses a filter tool to distinguish the liquid-vapor interface. These two videos show that annular flow is the dominant flow regime. Thin liquid wavy films exist on the periphery of the channels near the walls. Even though the liquid vapor interface is difficult to distinguish, the light and dark regions represent the vapor and liquid areas respectively. The entrance to the channels is on the top portion of the video, and the flow moves down the image. This video is played at 5 fps, 100 times slower than real time. Each of the videos can be accessed by clicking on the image.

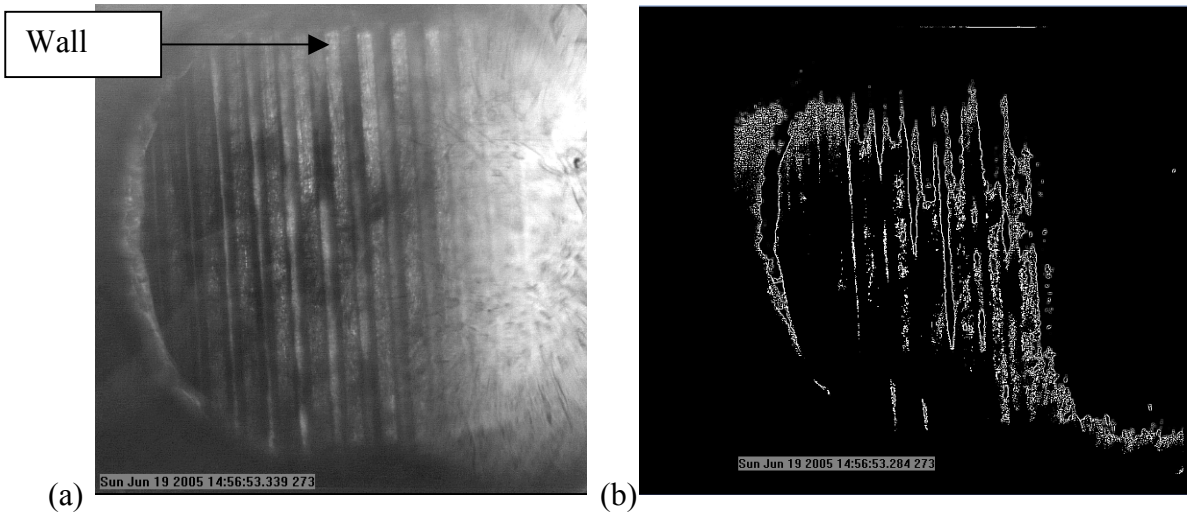

(a) (b)

Figure 20: Flow visualization of the micro-channel evaporator at 50 g/min and zero input power. (a) wadell_robert_p_200508_mast_fig20_annflow1.avi , 10 MB and (b) wadell_robert_p_200508_mast_fig20_annflow2.avi, 10 MB

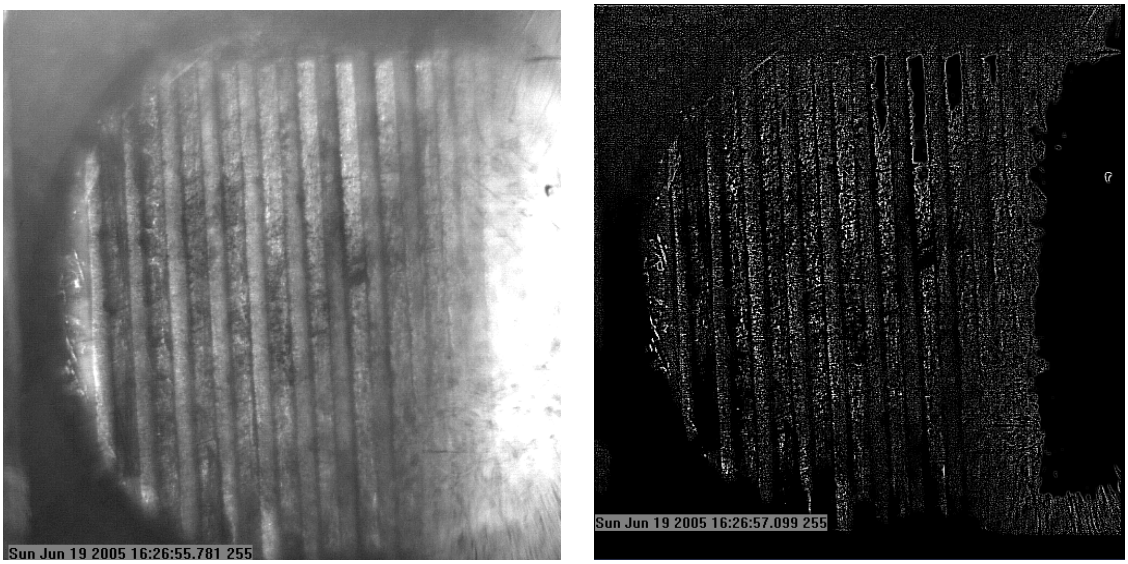

(a) (b)

Figure 21: Flow visualization of the micro-channel evaporator at 50 g/min and 70 W/cm^2. (a)wadell_robert_p_200508_mast_fig21_annflow.avi, 10 MB and (b) wadell_robert_p_200508_mast_fig21_annflow2.avi, 10 MB

When the power is increased from 60 W/cm^2 to 70 W/cm^2, the heat transfer coefficient rapidly decreases, as was mentioned in Section 4.2. The video shown in Figure 21 (a) and (b) captures refrigerant flowing at 50 g/min under a 70 W/cm^2 heat flux, and is played at

3.1 fps, 160 times slower than real time. These two videos show that at high heat fluxes, boiling occurs at the entrance to the micro-channel, causing a vapor bubble that enters the channel, pushes the liquid to the periphery, and entrains liquid droplets into the vapor core. Between these periods of dry out and entrainment, liquid fronts flow through the channels sporadically. Because of the absence of the thin liquid film on the wall, the maximum chip temperature increases from –68.3 ^{o}C to –50.5 ^{o}C, as shown in Figure 16.

4.4 Data Comparison with Micro-channel Correlations

Pressure drops and local heat transfer coefficients across the micro-channel evaporator were compared to predictions obtained from popular macro- and micro-channel correlations from the literature to determine which correlation best fit the data. Correlations were selected from a review paper by Kandlikar [16] and papers by Lee and Mudawar [17,18], which provide a comprehensive literature review of correlations for pressure drop and heat transfer in mini- and micro-channels. Kandlikar notes that heat transfer coefficient and pressure drop are highly dependent on the flow regimes inside the channel. Therefore, selection of correlations with similar flow regimes and conditions is critical in obtaining correct heat transfer and pressure drop predictions.

4.4.1 Pressure drop

Using the flow visualization map given by Taitel and Dukkler [19], the flow in our tests was predicted to be annular and was confirmed by flow visualization. Therefore, the separated flow model is the most accurate in predicting the pressure drops across the micro-channels (as opposed to the homogeneous flow model). The separated flow model

predicts that the pressure drop along the channel of a compact evaporator is a sum of frictional, gravitational, and accelerational pressure drops [15]:

$$-\left(\frac{dP}{dz}\right)=\left(\frac{1}{\Lambda}\right)\left[\Delta P_{fr}+\Delta P_{grav}+\Delta P_{acc}\right]=$$
$$\left(\frac{1}{\Lambda}\right)\left[\phi_l\left(\frac{2f_l G^2(1-x_e{}^2)}{\rho_l d_h}\right)+\left[(1-\alpha)\rho_l+\alpha\rho_v\right]g\sin\Omega+G^2\frac{dx}{dz}\left\{\left(\frac{2x_e}{\rho_g\alpha}-\frac{2(1-x_e)}{\rho_f(1-\alpha)}\right)+\frac{d\alpha}{dz}\left(\frac{(1-x_e)^2}{\rho_f(1-\alpha)^2}-\frac{x_e^2}{\rho_g\alpha^2}\right)\right\}\right] \quad (21)$$

Lockhart-Martinelli [20] proposed a two-phase frictional pressure multiplier, which is related to the purely liquid and vapor pressure gradients through friction multipliers that are dependent on vapor quality. Lee and Lee [21] and Lee and Mudawar [17] later proposed a modified form of the two-phase friction multiplier for use in rectangular micro-channels. For the conditions in the current study, the separated flow model predicts laminar liquid (Re_f<180) and turbulent vapor flows (Re_g>2840) over the entire channel. Therefore, a laminar liquid and turbulent vapor Martinelli parameter X was used. Because many of the correlations investigated pressure drop in circular channels, a friction factor, designed for single-phase flows in ducts of given aspect ratios β, was used [22]. Compressibility effects were ignored, $\Lambda = 1$ because the Mach number in the liquid and vapor flows was less than 0.3. A summary of the correlations and their conditions is given in Table 3and Table 4.

Table 3: Summary of relevant mini- and micro-channel pressure drop studies.

Investigator ***Type of Correlation***	**Fluid and Ranges of Parameters G (kg/m^{2}s), q" (kW/m^2) x_e Quality**	**Channel geometry, dimensions in mm, all horizontal**	**Flow Patterns**	**Remarks**
Current Study *Micro-channel*	R508b G=69-187 q"=59-294 x_e=0.34-0.87	13 parallel rectangular channels; L=10 13 channels 0.4 x 1.2 deep; 1 channel 10 by 1.2 deep	Annular flow	Laminar-liquid, turbulent vapor flow.
Lockhart-Martinelli *Macro-channel [20]*	Water, benzene, kerosene, oil, etc.	Single circular channels d_h=1.49-25.83	Bubbly, plug, slug, annular	Developed Lockhart-Martinelli parameter, which uses a two phase flow multiplier that is correlated to the local quality.
Lee and Lee 2001 *Micro-channel [21]*	Air and Water	4 single rectangular channels; 20 wide 0.4, 1 2, and-4 deep	Not observed.	Modified Martinelli parameter C to account for gap size.
Lee and Mudawar 2005 *Micro-channel [17]*	R-134, Water G=127-654 q"=31.6-93.8 x_e=0.26-0.87	54 parallel rectangular channels 0.213 x 0.713 deep L=25.3	Slugs, annular flow	Modified Martinelli parameter C to introduce Re_{fo} and We_{fo} to account for liquid breakup and deposition, which is influenced by surface tension.

Table 4: Two-phase frictional pressure drop correlations based on separated flow model for small channels.

Investigator ***Type of Correlation***	**Correlation**	**MAE % from Current Study**
Lockhart-Martinelli 1949 *Macro-channel [20]*	$\phi_f^2 = 1 + \frac{C}{X} + \frac{1}{X^2}$ $X = \left(\frac{f_f}{f_g}\right)^{0.5}\left(\frac{\rho_g}{\rho_f}\right)^{0.5}\left(\frac{1-x_e}{x_e}\right)$ For laminar liquid turbulent vapor conditions: $C = 12,\ f_f = \frac{f(\beta)}{\mathrm{Re}_f}\ f_{fo} = \frac{f(\beta)}{\mathrm{Re}_{fo}}, f_g = 0.079 \Big/ \mathrm{Re}_v^{0.25}$ $\mathrm{Re}_f = \frac{G(1-x_e)d_h}{\mu_f},\ \mathrm{Re}_{fo} = \frac{Gd_h}{\mu_f},\ \mathrm{Re}_g = \frac{Gx_e d_h}{\mu_g},$ $f(\beta) = 24\left(1 - 1.355\beta + 1.947\beta^2 - 1.702\beta^3 + 0.956\beta^4 - 0.254\beta^5\right)$	76.0
Lee and Lee 2001 *Micro-channel [21]*	$\phi_f^2 = 1 + \frac{C}{X} + \frac{1}{X^2}$ $C = c_1 \lambda^{c_2} \psi^{c_3} \mathrm{Re}_{fo}^{c_4}, \lambda = \frac{\mu_f^2}{\rho_f \sigma d_h}, \psi = \frac{\mu_f j_f}{\sigma}$ for laminar-liquid, vapor-turbulent conditions: $c_1 = 6.185\times10^{-2}, c_2 = 0, c_3 = 0, c_4 = 0.726$	29.9
Lee and Mudawar 2005 *Micro-channel [17]*	$\phi_f^2 = 1 + \frac{C}{X} + \frac{1}{X^2}$ $C = c_1 \mathrm{Re}_{fo}^{c_2} We_{fo}^{c_3}$ For laminar-liquid, turbulent-vapor conditions: $c_1 = 1.45, c_2 = 0.25, c_3 = 0.23$	36.6

There are also associated expansion and contraction pressure drops in a micro-channel evaporator when manifolds are used to distribute the refrigerant into and out of the channels [23]:

$$\Delta P_e = \frac{G_o^2}{2}(1-\sigma)^2 v_f \left[1+\left(\frac{v_{fg}}{v_f}\right)x_o\right] \tag{22}$$

$$\Delta P_c = \frac{G_i^2}{2}\left[\frac{1}{C_c}-1\right]^2\left[1+\left(\frac{v_{fg}}{v_f}\right)x_i\right] \tag{23}$$

If the vapor at the exit of the micro-channel is superheated, than the exit quality should be set to unity. Because the channels are horizontal, the gravitational pressure drop is zero. Therefore, the total pressure drop across the inlet and outlet of the channels is the sum of the contraction, expansion, frictional, and accelerational pressure drops:

$$\Delta P = \Delta P_{chan} + \Delta P_e + \Delta P_c \text{ where} \tag{24}$$

$$\Delta P_{chan} = \int_{z_o}^{z_i} \phi_l \left(\frac{2 f_l G^2 (1-x_e{}^2)}{\rho_l d_h}\right) + G^2 \frac{dx}{dz}\left\{\left(\frac{2x_e}{\rho_g \alpha} - \frac{2(1-x_e)}{\rho_f (1-\alpha)}\right) + \frac{d\alpha}{dz}\left(\frac{(1-x_e)^2}{\rho_f (1-\alpha)^2} - \frac{x_e^2}{\rho_g \alpha^2}\right)\right\} dz \tag{25}$$

Equation 24 was used to compute the total pressure drop along the channel. The first-order Euler method was used to numerically integrate equations 25 from outlet to inlet to obtain the frictional and accelerational pressure drops. Figure 22 shows a comparison of the measured pressure drop to the predicted pressure drops from the correlations.

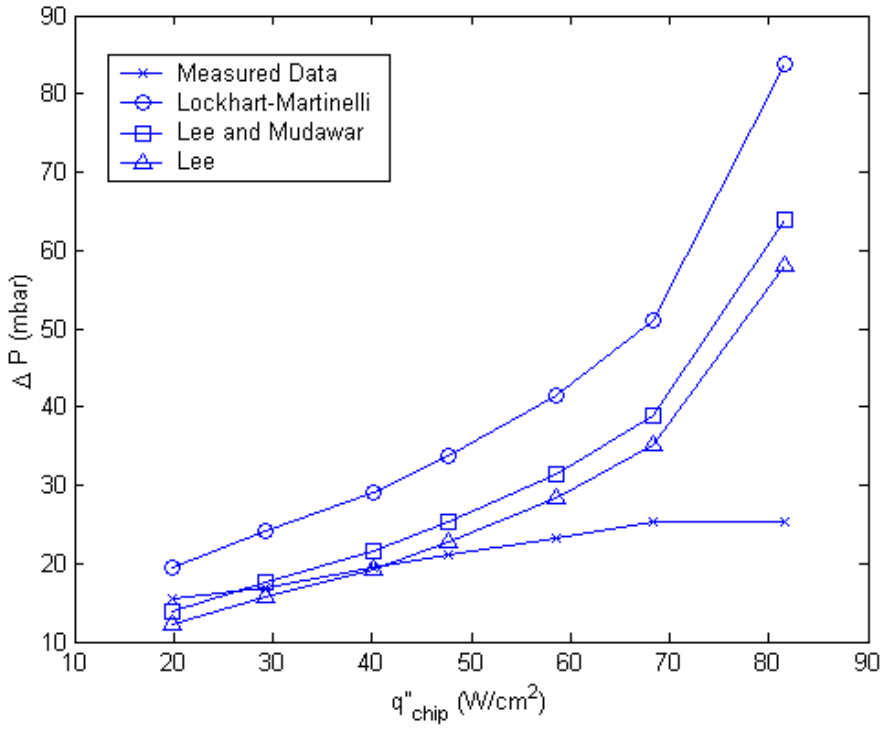

Figure 22: Measured and predicted pressure drops vs. heat flux in micro-channels, at 60 g/min.

The correlations over predict the pressure drops that were measured, with the micro-channel two-phase flow multipliers (Lee and Lee, and Lee and Mudawar) yielding more accurate results. The pressure drop increases as heat flux is increased up to 70 W/cm^2, and then decreases at higher heat fluxes, mainly due to the decrease of frictional pressure drop at 80 W/cm^2. This trend can be explained by examination of the various components of the pressure drop, as shown in Figure 23.

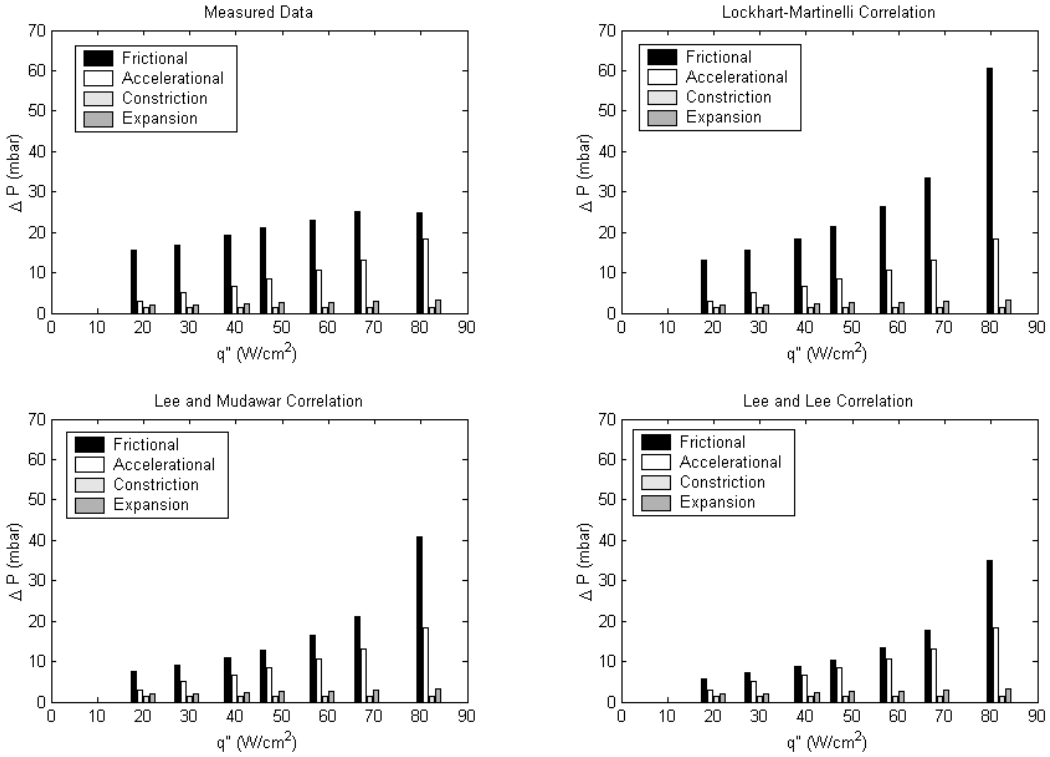

Figure 23: Frictional, accelerational, constriction, and expansion components of pressure drop at 60 g/min.

A critical heat flux condition due to dry out, such as an entrainment of liquid into the vapor core over the majority of the channel, would detach the liquid from the wall and cause a decrease in the frictional pressure drop at 80 W/cm^2. Even though there was no flow visualization at this data point to confirm dry out, the heat transfer measurements indicate dry out due to a rapid increase in maximum chip temperature, as shown in Figure 16. Lee and Mudawar also reported a decrease in the pressure drop at high heat fluxes (q"> 60 W/cm^2), however their correlation does not predict a decrease in pressure drop for q"=70 to 80 W/cm^2 in the current study. Assuming the 30 W of heat leak in the current study was inputted directly into the 1 cm^2 of micro-channels, the correlations would predict even higher pressure drops than those shown in Figure 22.

Figure 24 shows the predicted pressure drops using various correlations, versus the measured pressure drops for all 22 data points. Correlations of Lee and Lee had the best agreement with the present data, at a MAE of 29.9%, as shown in Table 5.

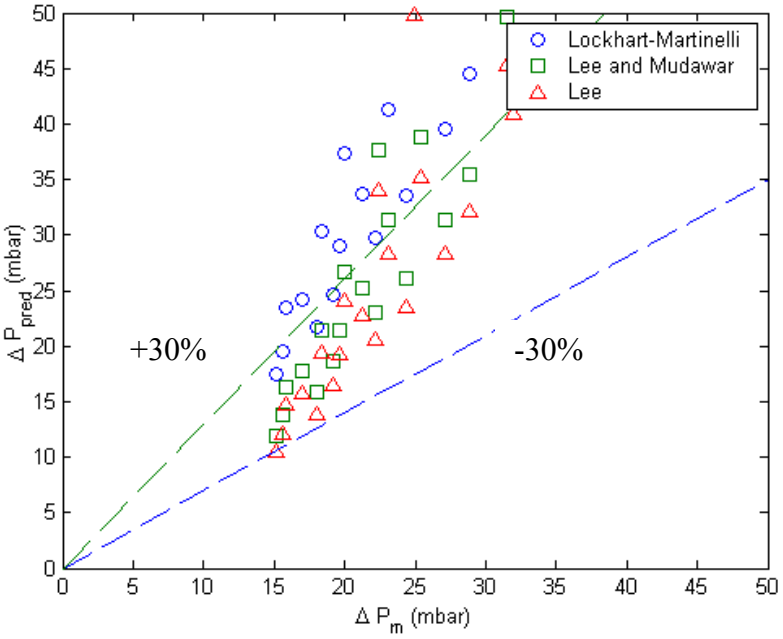

Figure 24: Comparison of measured and predicted pressure drops, without heat leak.

Table 5: Mean absolute errors for macro and micro-channel pressure drop correlations.

Correlation	Lockhart-Martinelli [20]	Lee and Lee [21]	Lee and Mudawar [17]
MAE%	76.0	29.9	36.6

4.4.2 Local heat transfer coefficient

Figure 25 shows the effect of heat flux and quality on the heat transfer coefficient at three stream-wise locations ($T_{m,W}$, $T_{m,Y}$, $T_{m,Z}$) at 50 g/min. For the same heat flux, the heat

transfer coefficient slightly decreases with increasing quality, showing that h_m is almost independent of quality. At a flow rate of 50 g/min, increasing the heat flux q" increases the heat transfer coefficient h_m only up to 40 W/cm^2, after which h_m decreases with q", indicating partial dry out. At higher flow rates, higher heat fluxes can be attained before this inversion point occurs, indicating that partial dry out is delayed with higher mass fluxes. Partial dry out can be confirmed for q"=70 W/cm^2 by watching the video shown in Figure 21.

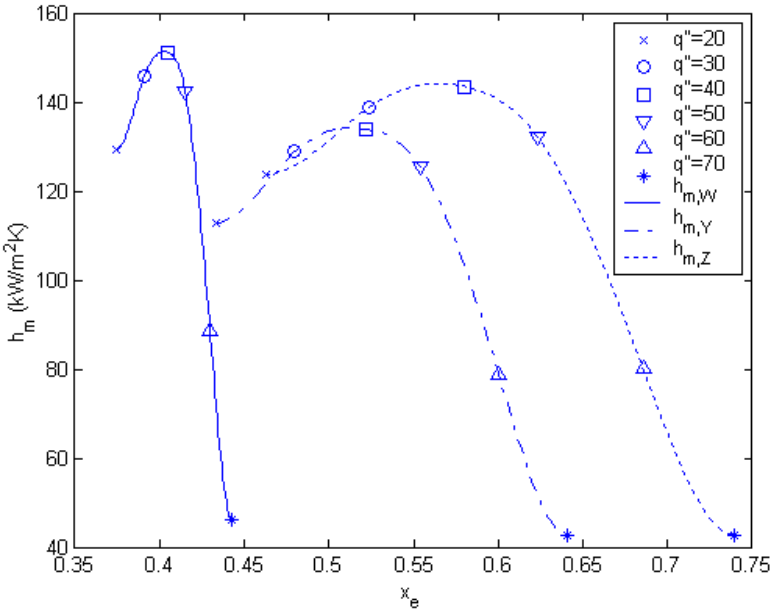

Figure 25: Variation of heat transfer coefficient with heat flux and quality at 50 g/min.

Table 6 and Table 7 show a summary of micro-channel heat transfer correlations and their conditions that were most applicable to the current study. The macro-channel correlations [24-26] are generally used for 2 mm diameter size channels and above, where turbulent vapor and turbulent liquid conditions exist. The laminar liquid and turbulent vapor Martinelli parameter, X , was used in order to predict local heat transfer

coefficient in micro-channels. Also, many of the correlations were developed using circular channels. To account for the effect of a rectangular geometry, Nusselt numbers [22] were used for ducts of a given aspect ratio β to determine single-phase heat transfer coefficients.

The micro-channel correlations [27-29,18] involved studies of refrigerants and fluorocarbons in rectangular channels. The most similar in fluid properties, heat flux, and channel length to the current study is the correlation by Lee and Mudawar.

Table 6: Summary of relevant mini- and micro-channel heat transfer studies.

Investigator ***Type of Correlation***	**Fluid and Ranges of Parameters G (kg/m^2s), q" (W/cm^2) x_e Quality**	**Channel geometry, dimensions in mm, all horizontal**	**Flow Patterns**	**Remarks**
Current Study *Micro-channel*	R508b G=69-187 q"=20-100 x_e=0.34-0.87	13 parallel rectangular channels; L=10 13 channels 0.4 x 1.2 deep; 1 channel 10 by 1.2 deep	Annular flow	Laminar liquid (Re_f<500) and turbulent vapor (Re_v>1500) flow over majority of channel. Convective heat transfer, which is highly dependent on mass flux, and high void fraction indicates annular flow.
Tran 1996 *Mini-channel* [27]	R12 G=44-832 q"=3.6-12.9 x_e=0-0.96	Circular D_h=2.46 Rectangular D_h=2.40 L=870	Not studied	Nucleate boiling and convective heat transfer.
Lee and Lee 2001 *Micro-channel* [28]	R113 G=50-200 q=0.3-1.58 x_e=0.15-0.75	3 single rectangular channels; 20 wide 0.4-2 deep	Not observed	Forced convective boiling. Laminar liquid, turbulent vapor. Increasing heat transfer coefficient with quality.
Warrier 2002 *Micro-channel* [29]	FC84 G=557-1600 q"=0-5.99 x_e=0.03-0.5	5 parallel rectangular channels D_h=0.75 L=307.4	Not observed	Heat transfer was dependent on q" and x_e.
Lee and Mudawar 2005 *Micro-channel* [18]	R-134 G=127-654 q"=15.9-93.8 x_e=0.26-0.87	54 parallel rectangular channels 0.213 x 0.713 deep L=25.3	Slugs, annular flow	Laminar liquid, vapor is turbulent in R134a and laminar in water b/c of viscosity. Decreasing heat transfer coefficient with quality.

Table 7: Previous correlations for boiling in small channels.

Investigator	Correlation
Schrock 1959 [24]	$h_{tp} = \left(\frac{Nu_3}{Nu_4}\right) E h_{sp,f}$, $E = 0.00739\left(Bo + 1.5E - 4\left(\frac{1}{X}\right)^{0.66}\right)$ $Bo = \frac{q''}{Gh_{fg}}$ $\quad X = \left(\frac{f_f}{f_g}\right)^{0.5}\left(\frac{1-x_e}{x_e}\right)\left(\frac{\rho_g}{\rho_f}\right)^{0.5}$ $h_{sp,f} = Nu_f \frac{k_f}{d_h}$ $\quad Nu_{f,lam} = const$ $\quad \beta = \frac{W_{ch}}{H_{ch}}$ For laminar-liquid, turbulent-vapor: $f_f = 64/\mathrm{Re}_f$, $f_g = 0.079/\mathrm{Re}_g^{0.25}$ $Nu_3 = 8.235(1 - 1.883\beta + 3.767\beta^2 - 5.814\beta^3 + 5.361\beta^4 - 2.0\beta^5)$ $Nu_4 = 8.235(1 - 2.042\beta + 3.085\beta^2 - 2.477\beta^3 + 1.058\beta^4 - 0.186\beta^5)$
Shah 1982 [25]	$h_{tp} = \left(\frac{Nu_3}{Nu_4}\right) Max(E, S)\, h_{sp,f}$ For 1.0<N, S=1.8/N$^{0.8}$, $E = 230Bo^{0.5}$ for $Bo > 3\times10^{-5}$ or $E = 1 + 46Bo^{0.5}$ for $Bo < 3\times10^{-5}$ For $0.1 < N \le 1.0, S = 1.8/N^{0.8}, E = FBo^{0.5}\exp\left(2.74N^{-0.1}\right)$ For $N \le 0.1, S = 1.8/N^{0.8} E = FBo^{0.5}\exp\left(2.47N^{-0.15}\right)$ $F = 14.7$ for $Bo \ge 11\times10^{-4}$ or $F = 15.43$ for $Bo < 11\times10^{-4}$ $N = Co$ for $Fr_f \ge 0.04$ or $N = 0.38Fr_f^{-0.3}Co$ for $Fr_f < 0.04$ $Co = \left(\frac{1-x_e}{x_e}\right)^{0.8}\left(\frac{v_f}{v_g}\right)^{0.5}$, $Fr_f = \frac{v_f^2 G^2}{g d_h}$
Gungor-Winterton 1986 [26]	$h_{tp} = \left(\frac{Nu_3}{Nu_4}\right) E h_{sp,f}$, $\quad E = 1 + 3000Bo^{0.86}\left(\frac{x_e}{1-x_e}\right)^{0.75}\left(\frac{\rho_f}{\rho_g}\right)^{0.41}$
Tran 1996 [27]	$h_{tp} = \left(\frac{Nu_3}{Nu_4}\right) 8.4\times10^{-5}\left(Bo^2 We\right)^{0.3}\left(\frac{\rho_f}{\rho_g}\right)^{-0.4}$, $We_{fo} = \frac{v_f G^2 d_h}{\sigma}$
Lee and Lee 2001 [28]	$h_{tp} = \left(\frac{Nu_3}{Nu_4}\right) E h_{sp,f}$, $E = 10.3\beta^{0.398}\phi_f^{0.598}$, $\phi_f^2 = 1 + \frac{C}{X^2} + \frac{1}{X^2}$, $C = 6.185\times10^{-2}\,\mathrm{Re}_{fo}^{0.726}$
Warrier 2002 [29]	$h_{tp} = \left(\frac{Nu_3}{Nu_4}\right) E h_{sp,f}$, $E = 1.0 + 6Bo^{1/16} + f(Bo)\, x_e^{0.65}$, $f(Bo) = -5.3(1 - 855Bo)$
Lee and Mudawar 2005 [18]	$0.05 < x_e < 0.55$ $\quad h_{tp} = E h_{sp,f}$, $E = 436.48Bo^{0.522}We_{fo}^{0.351}X^{0.665}$ $0.55 < x_e < 1.0$ $\quad h_{tp} = \max\left\{(108.6X^{1.665}h_{sp,g}), h_{sp,g}\right\}$ $h_{sp,g} = 0.023\,\mathrm{Re}_g^{0.8}\,\mathrm{Pr}_g^{0.4}$ for turbulent gas flow

Figure 26 shows a comparison between the calculated heat transfer coefficient 6 mm from the entrance of the channel at thermocouple Y (see Figure 6) and the predicted heat transfer coefficients from various correlations at $\dot{m}$ =50 g/min and q" = 20-130 W/cm^2.

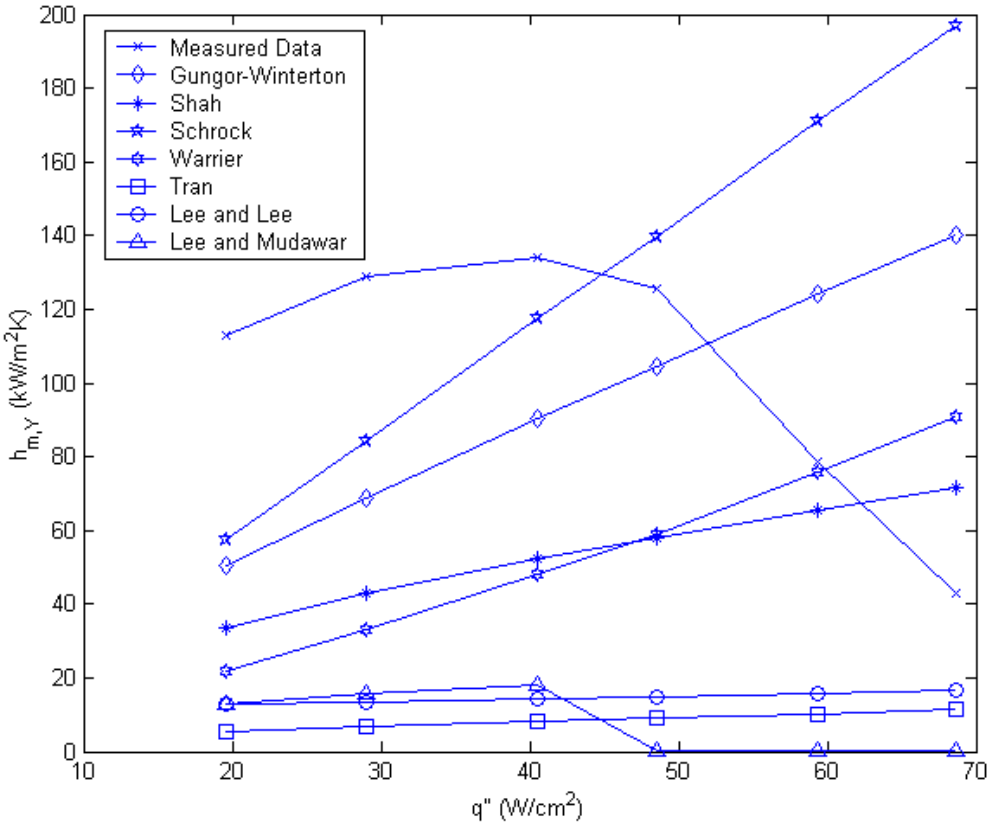

Figure 26: Measured and predicted heat transfer coefficient vs. heat flux in micro-channels, without heat leak.

As heat flux is increased from 20-100 W/cm^2, the local quality at thermocouple Y increases from 0.42-0.66. Every correlation except for Lee and Mudawar shows that the heat transfer coefficient will increase with heat flux, despite the increase in quality from 0.42-0.66. Here the effect of heat flux is stronger than the effect of increasing qualities. The correlation by Lee and Mudawar predicts the heat transfer coefficient increasing with

heat flux, until dry out is predicted at thermocouple Y at a quality of 0.55, which closely matches the trend with the measured data. The trends of the correlations are also captured by the remarks in Table 6.

The poor comparison between the correlations and the current experimental data can be explained when their ranges of dimensionless parameters Bo, We, X^2 are compared to the conditions of the current study (see Figure 27 and Table 8). In the current study, correlations predict that the effect of heat flux is more pronounced than quality, leading to an increasing heat transfer coefficient. This effect of the heat flux on the heat transfer coefficient may be more pronounced at low Boiling numbers ($Bo < 0.005$), however at high Boiling numbers the mass flux may not accommodate the heat flux in the channel walls, leading to dry out over portions of the walls and a gradual decrease in heat transfer coefficient with heat flux at lower qualities than other investigations.

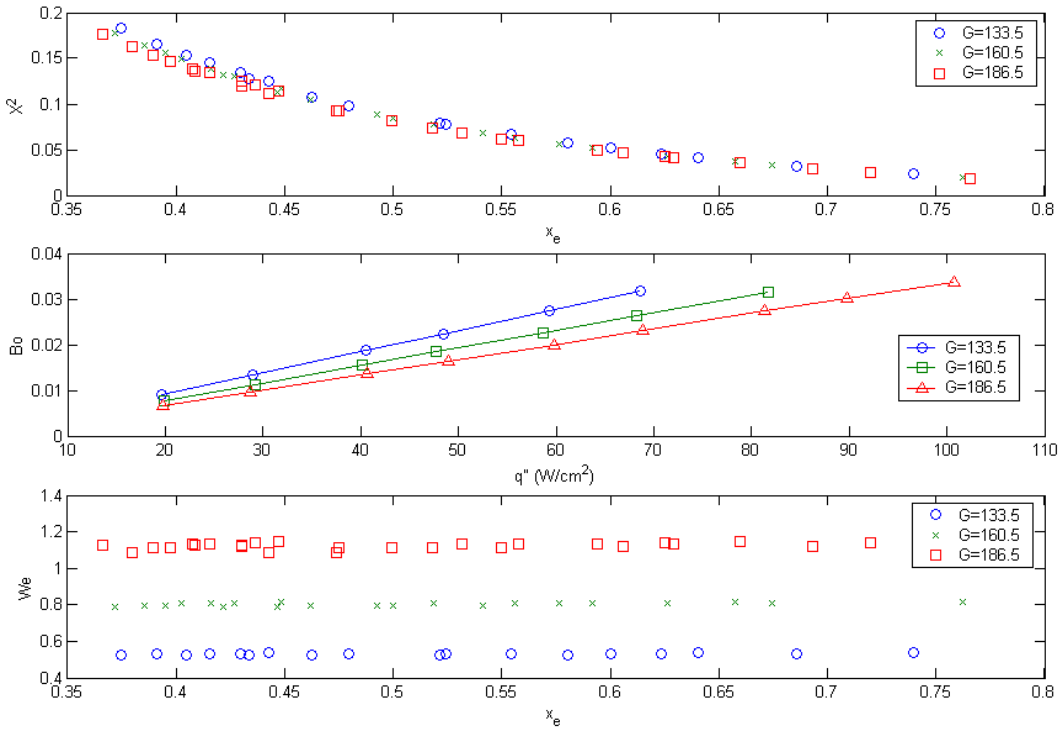

Figure 27: (a) Martinelli parameter, (b) Boiling number, and (c) Weber number vs. quality at various mass fluxes.

Table 8: Comparison of dimensionless parameter ranges in current study to past correlations.

Dimensionless Parameters in Correlations	Range of Previous Correlations	Range of Current Study
Bo	<0.005	0.007-0.034
X^2	0.2-1	0.14-0.43
We_{fo}	0.1-16	0.53-1.15

Figure 28 shows that on average, all of the correlations under-predicted the heat transfer coefficient. For all 66 data points recorded from thermocouples W,Y, and Z, the macro-

channel correlations fit the data better than the micro-channel correlations, as sho in Table 9.

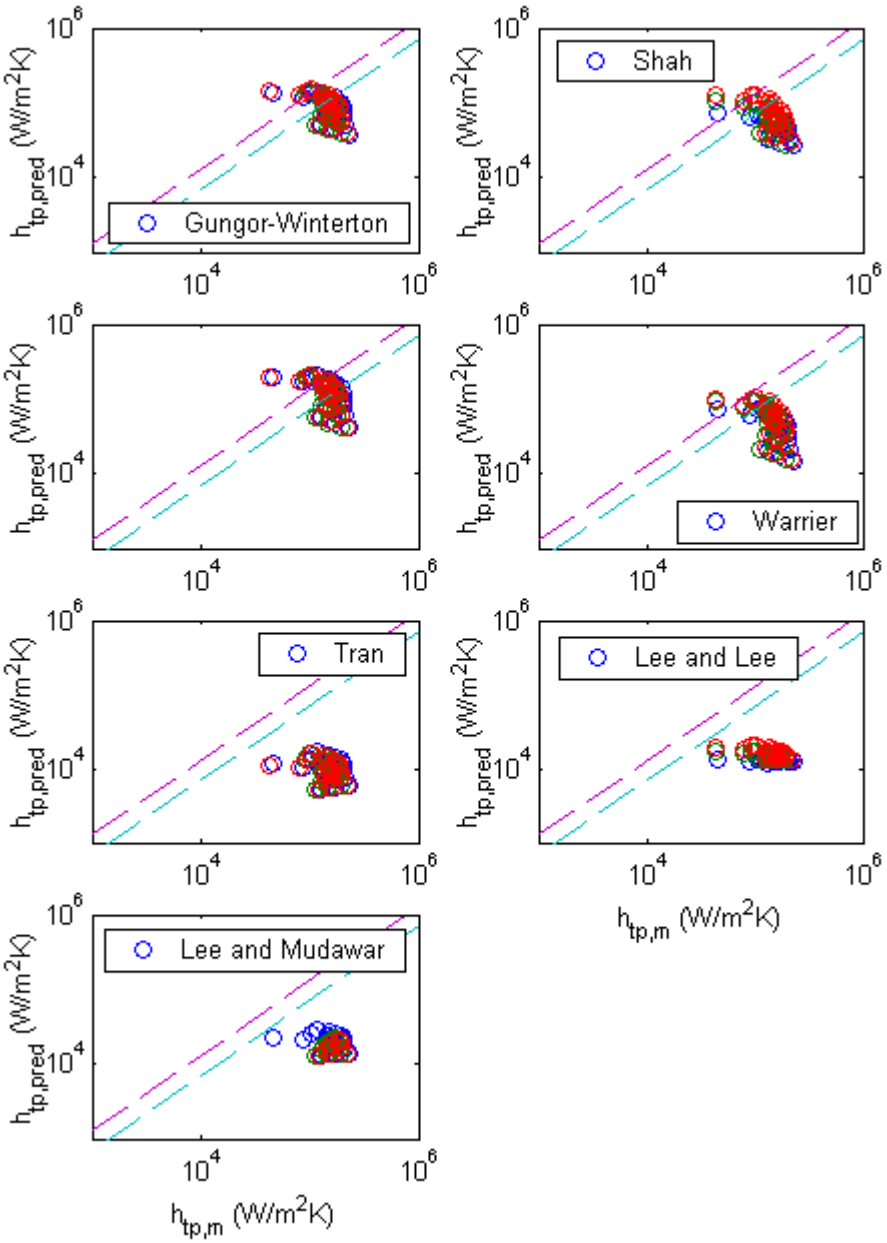

Figure 28: Comparison of measured and predicted heat transfer coefficients, without the heat leak.

Table 9: Mean absolute errors in heat transfer coefficient without the heat leak.

Investigator	**MAE%**
Schrock 1959 *Macro-channel*	60.7
Shah 1982 *Macro-channel*	61.6
Gungor-Winterton 1986 *Macro-channel*	54.2
Tran 1996 *Mini-channe*l	92.0
Lee and Lee 2001 *Micro-channel*	88.6
Warrier 2002 *Micro-channel*	65.0
Lee and Mudawar 2005 *Micro-channel*	91.6

The comparisons shown in Figure 28 were made on the assumption that there was no heat leak into the evaporator. However, because an energy balance on the system determined that there was approximately 30 W of heat leak from the ambient between the sub-cooled state T_4 and superheated state T_6 (see Figure 4), the heat transfer coefficient reported were conservative values. Assuming that the entire heat leak enters the micro-channels inside the evaporator, than an additional 30 W/cm^2 of heat flux would increase the heat transfer coefficients reported in Figure 25, yielding higher evaporator performance.

CONCLUSION

This paper was a study focused on characterizing the performance of compact micro-channel and inline/alternating pin fin evaporators for ultra low temperature refrigeration of microprocessors. Experimental results from the compact evaporators were discussed, complemented by the design of a micro-channel evaporator using macro and micro-channel correlations. Key findings from this study are as follows:

(1) Of all the evaporators considered, the alternating micro-pin fin provided the lowest chip temperatures, especially at high heat fluxes. For example, at 100 W/cm^2 the alternating pin maintained a –63 ^oC maximum chip temperature, approximately 13 ^oC lower than the baseline geometry. Despite having the largest pressure drop, it is the recommended design.

(2) The evaporators with micro-channels and micro pin fins performed significantly better than the baseline evaporator. However, this performance enhancement was due to an increase in the contact area (A_w) between the refrigerant and the evaporator. The effective heat transfer rates of the micro-channel and micro pin fin evaporators were actually lower than the baseline when the contact area was taken into account.

(3) Pressure drop in all of the evaporators in the current study was below 250 mbar, which caused negligible changes in the average saturation temperature. When using R508b as the evaporating fluid, pressure drops should be maintained below 1 bar, otherwise temperature glides will cause significant increases in the chip temperature.

(4) Flow visualization confirmed that the flow regime was annular throughout the micro-channel for the lowest flow rate of 50 g/min. The heat transfer was highly dependent on mass flux, indicating that forced convective heat transfer due to annular flow was the dominant heat transfer mechanism. Bubble nucleation was not observed inside the channels, however this could be due to poor flow visualization quality. Further work is required to enhance video quality.

(5) For the micro-channel evaporator, quality had a negligible effect on the heat transfer coefficient, whereas heat flux had a strong influence. The frictional pressure drop decreased at high qualities, due to entrainment of the liquid into the vapor flow.

(6) For the micro-channel evaporator, the Gungor-Winterton correlation was the most accurate in predicting local heat transfer coefficients, with a MAE of 54.2. The Lee and Lee correlation was the most accurate in predicting pressure drops, with a MAE of 29.9%. In general, the correlations under predicted the heat transfer, and over predicted the pressure drops.

(7) Rubber o-ring and gasket materials such as viton, buna-n, and neoprene lose their sealing properties below –50 ^{o}C temperatures. Plastics such PTFE must be used for sealing at –80 ^{o}C and cannot be re-used or re-compressed due to permanent deformation.

(8) Visualization of ultra low temperature refrigerants and cryogenic fluids is challenging. Care must be taken when designing a test module that allows optical access to the flow.

(9) Radiation shielding and effective foam insulation are required to reduce the effects of heat leaks when interfacing a two-phase VCR system and a microprocessor. Ice build up on the electronic components is expected unless the air is dehumidified or nitrogen purged from the computer case. Vacuuming the surrounding air is a feasible option for insulation and de-humidification, however this makes electronics packaging difficult.

APPENDIX A: SOLIDWORKS DRAWINGS

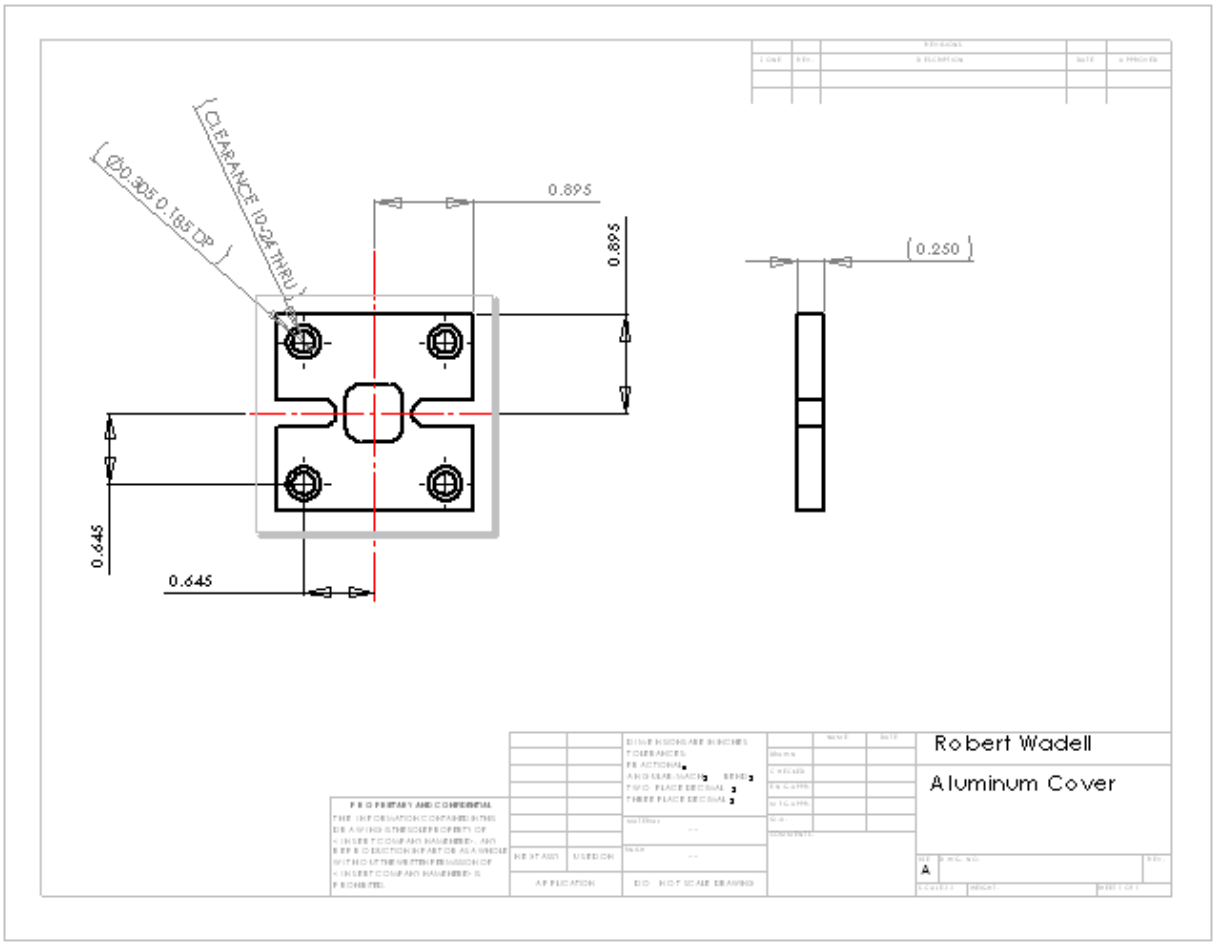

Figure A1: Aluminum cover layout.

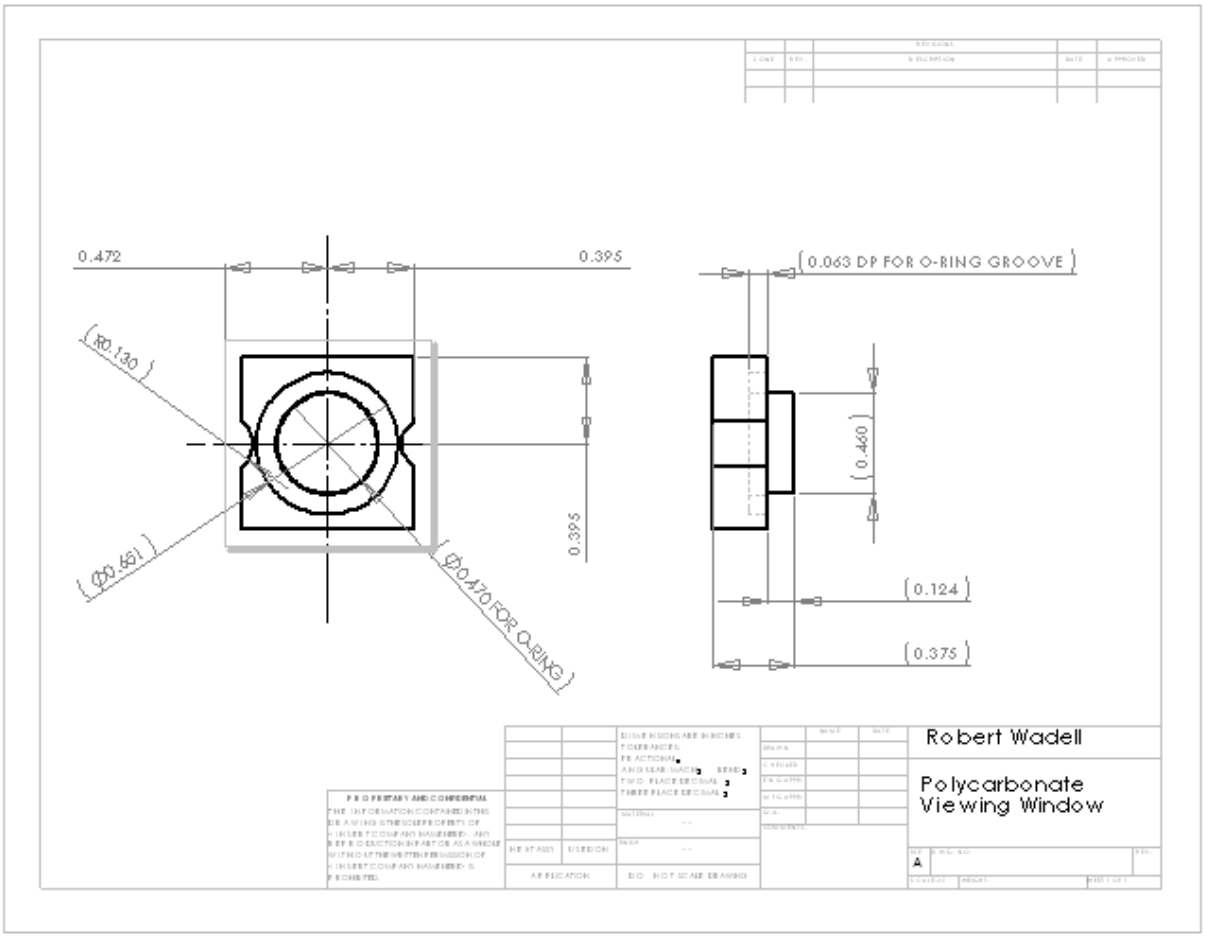

Figure A2: Polycarbonate Viewing Window Layout

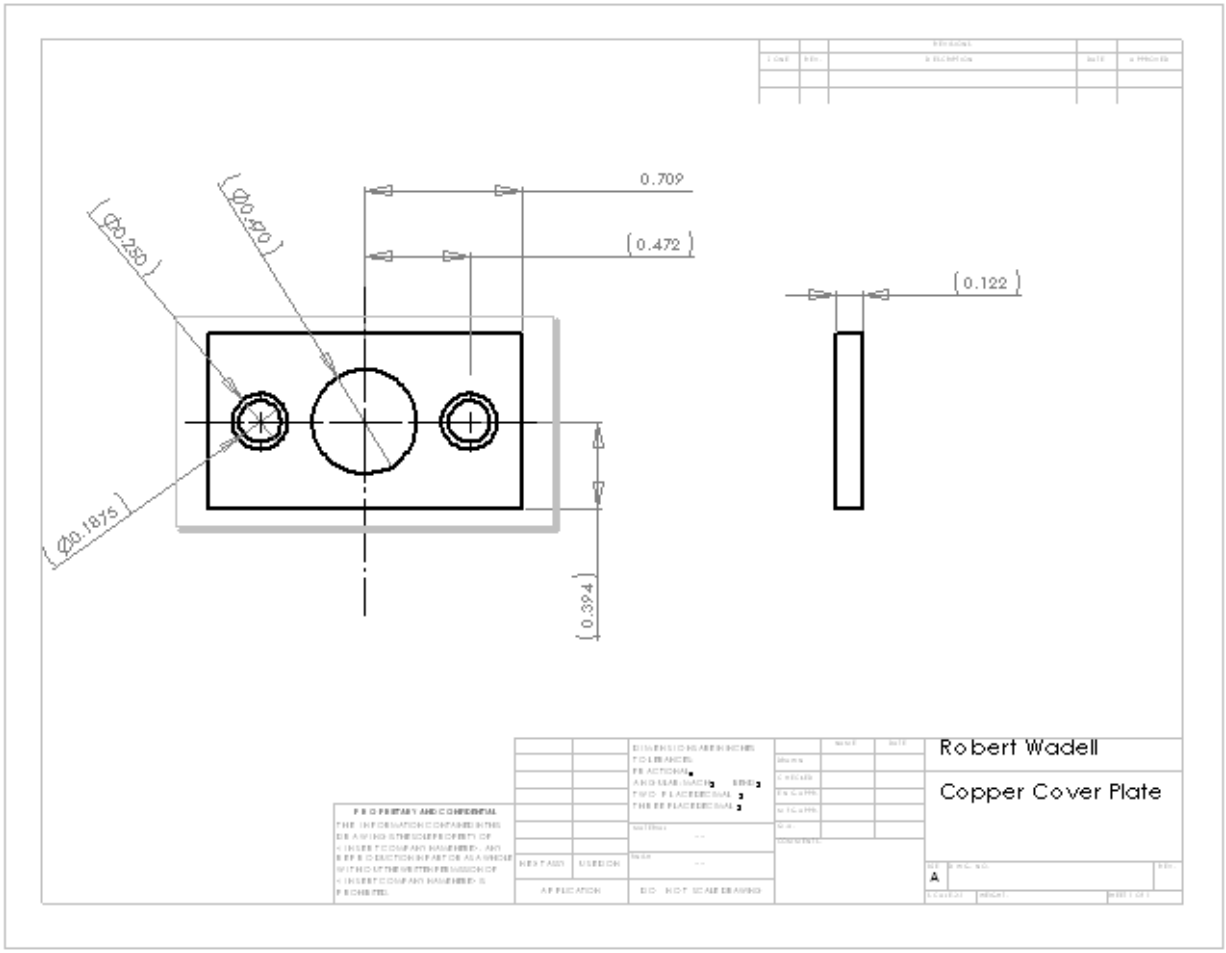

Figure A3: Copper Cover Plate Layout

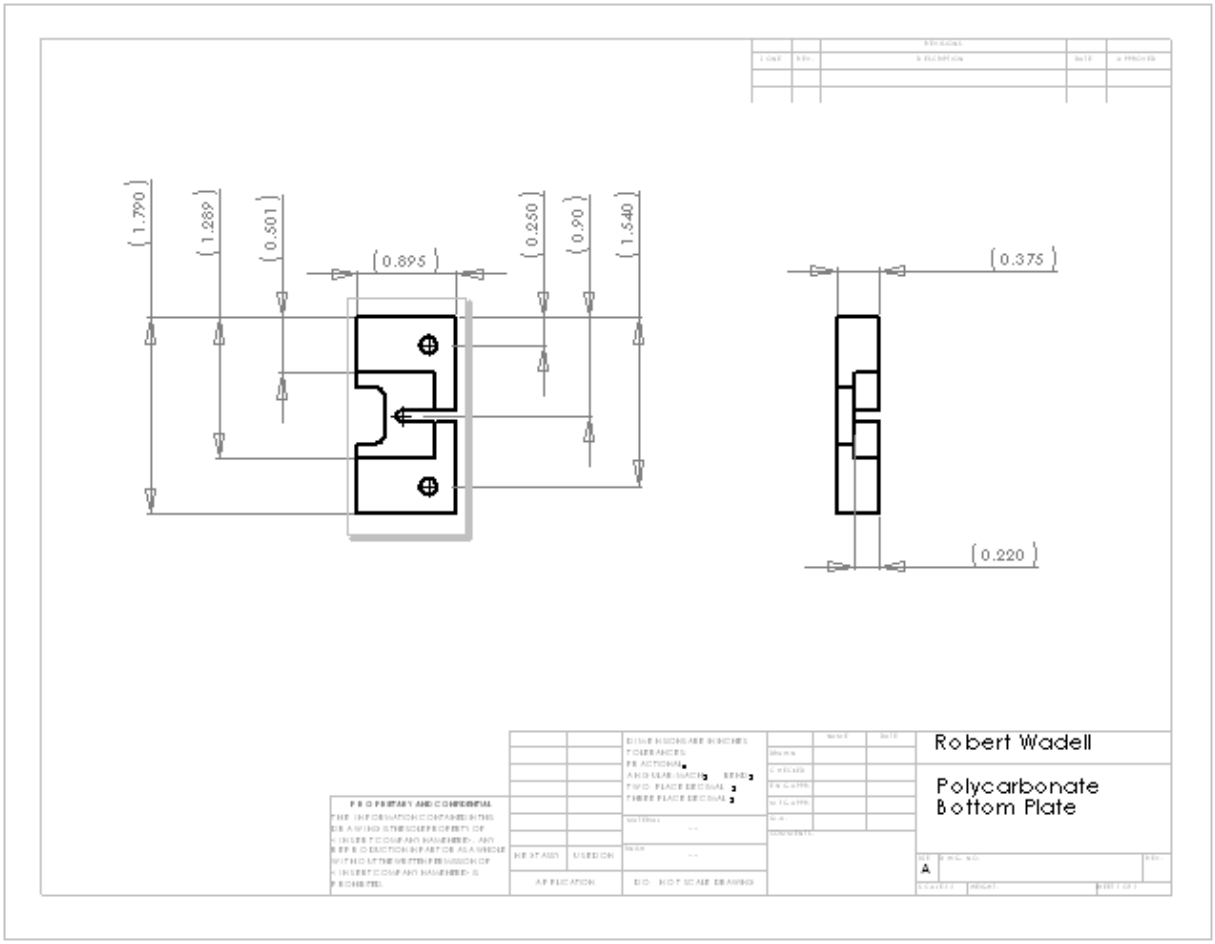

Figure A4: Polycarbonate Bottom Plate Layout

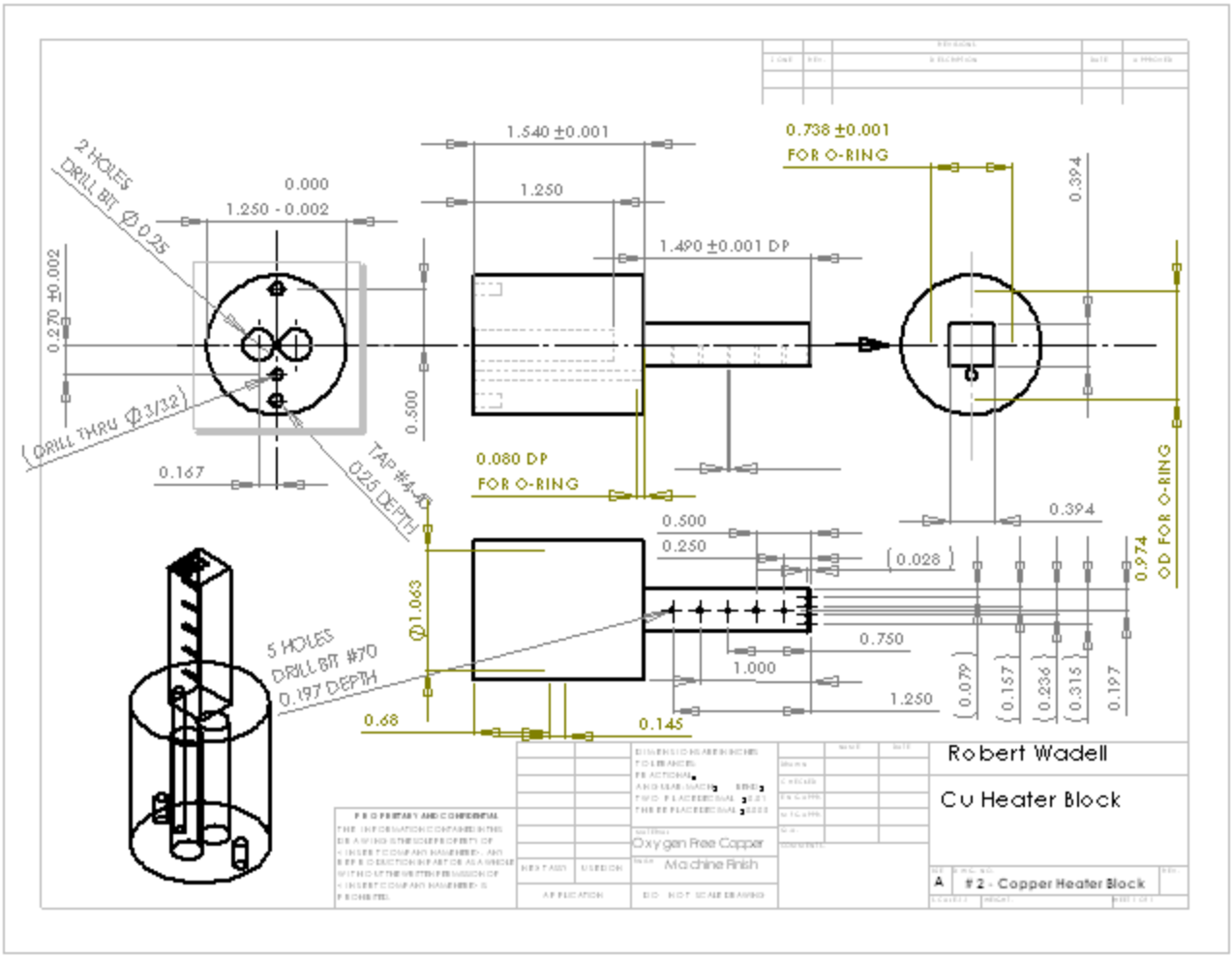

Figure A5: Copper Heater Block Layout

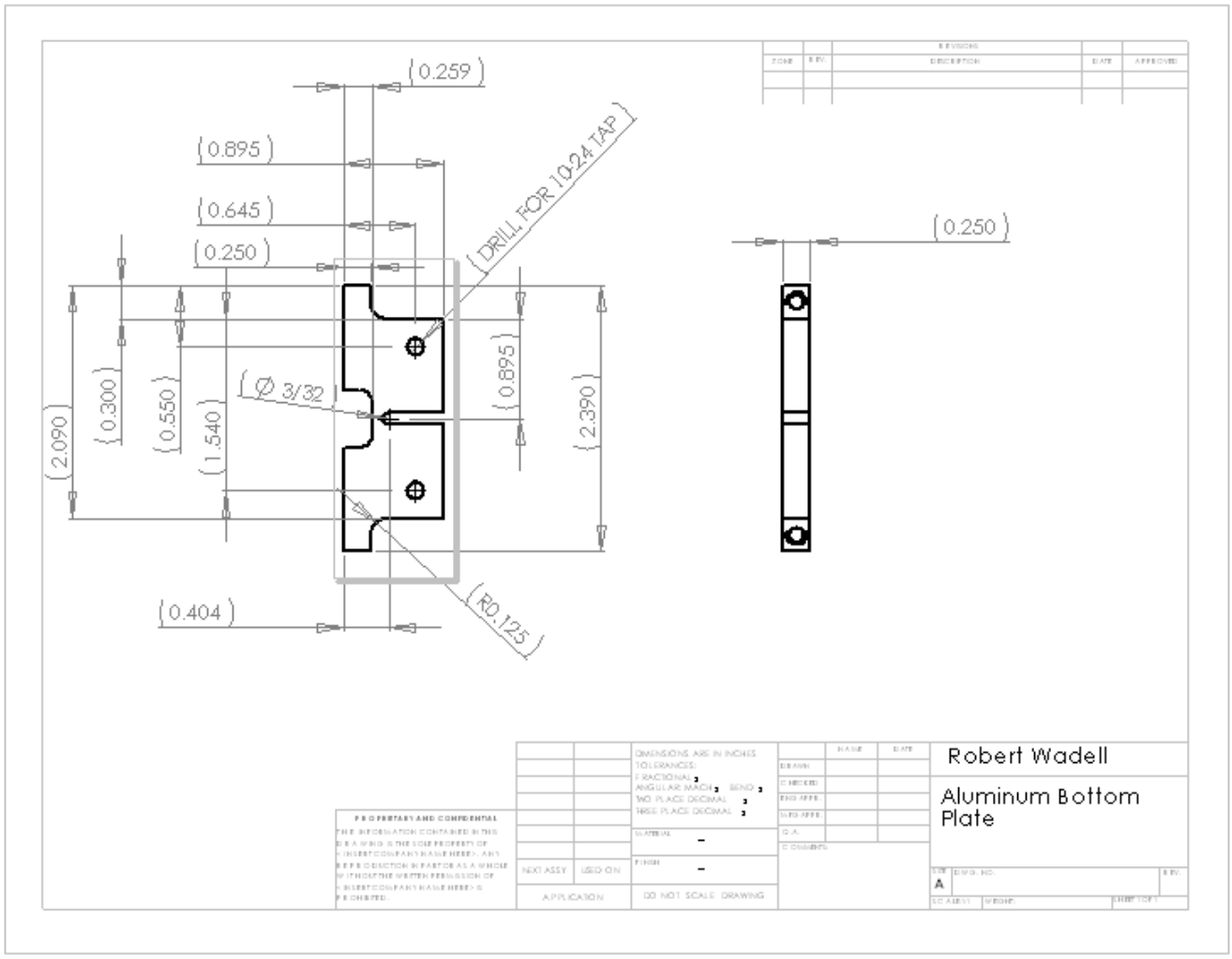

Figure A6: Aluminum Bottom Plate Layout

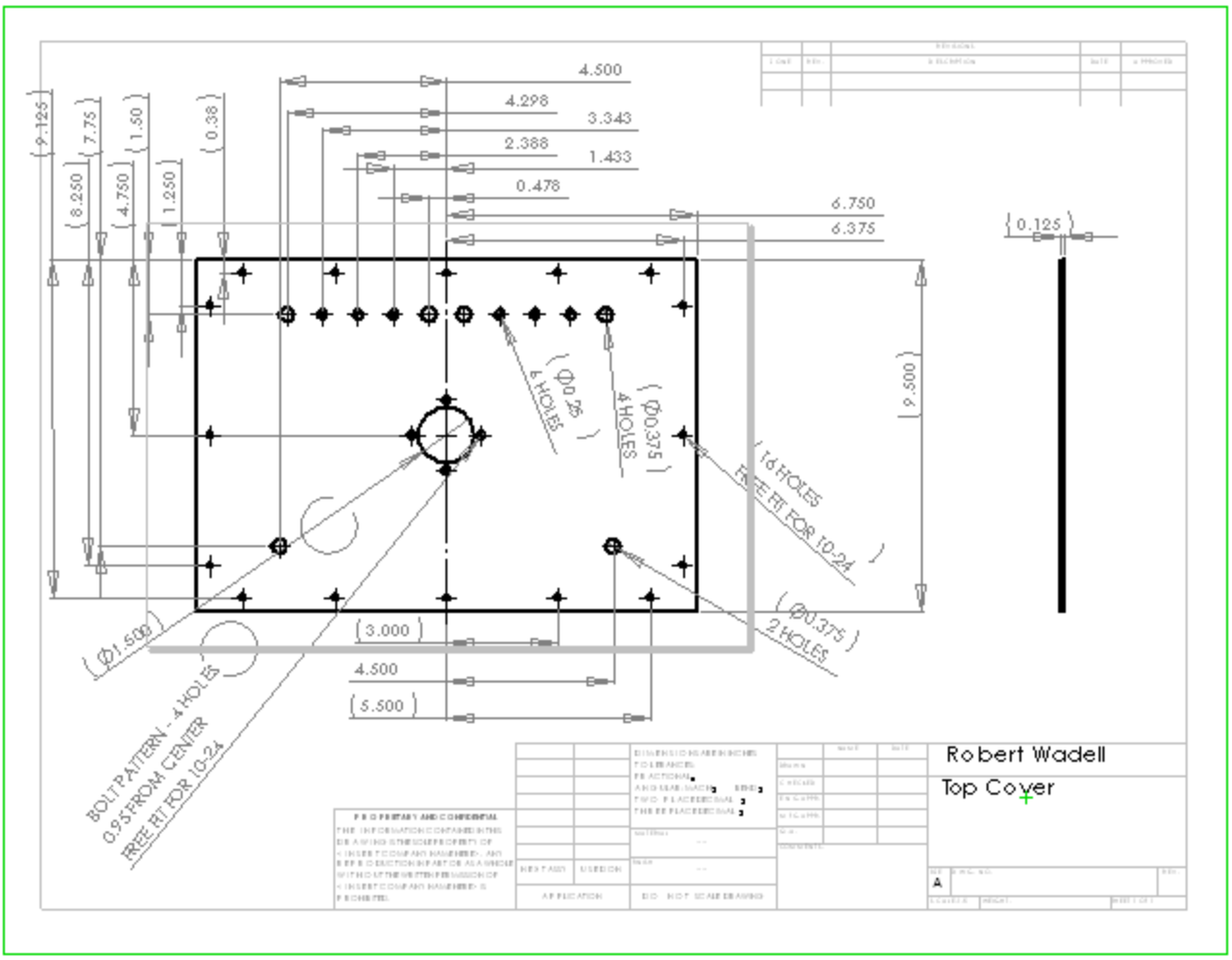

Figure A7: Top Cover Layout

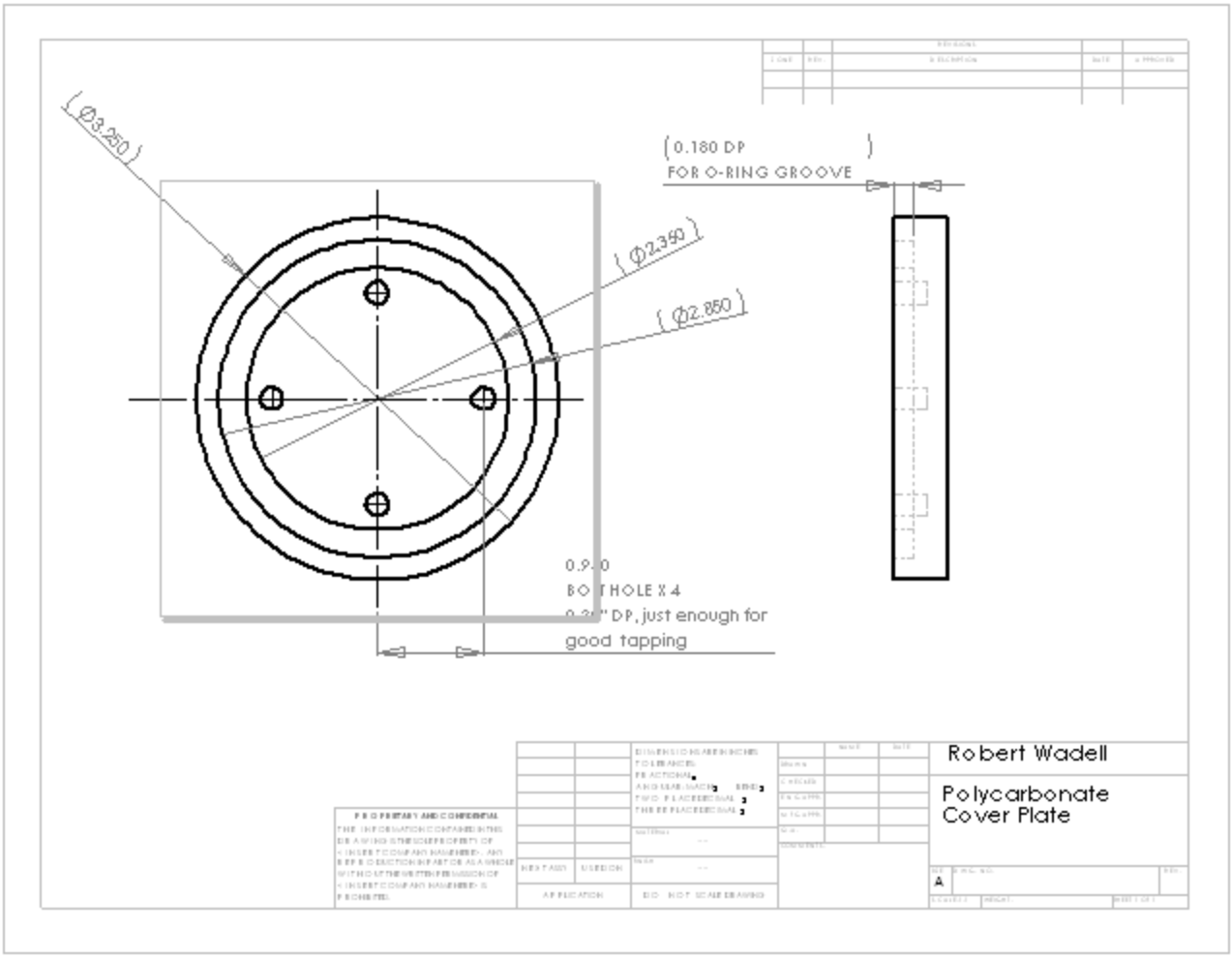

Figure A8: Polycarbonate Cover Plate Layout

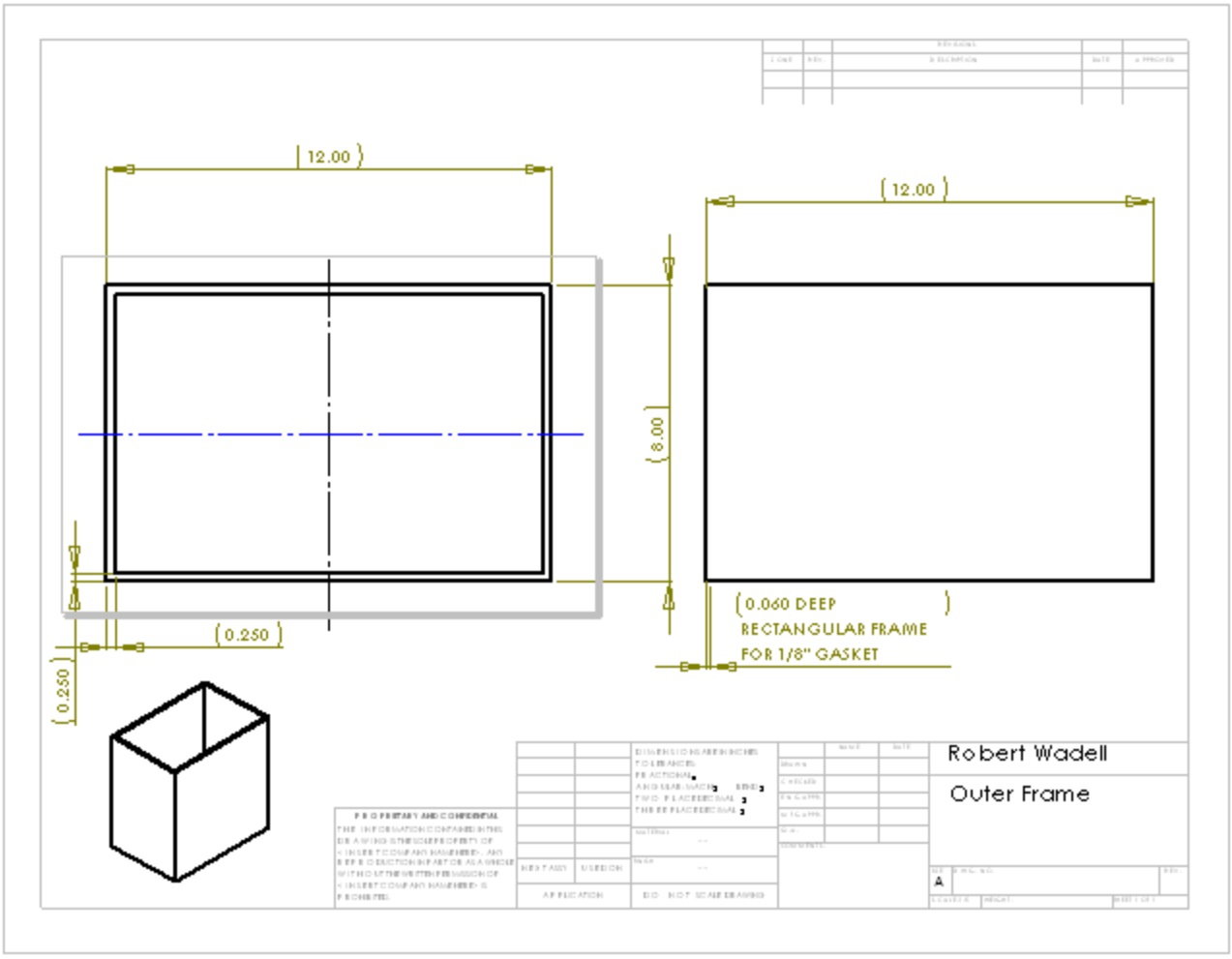

Figure A9: Outer Frame Layout

BIBLIOGRAPHY

[1] International Technology Roadmap for Semiconductors, 2004 ed., Semi-conductor Industry Association, 2004

[2] Cryomech, Inc., Product List, Accessed April 2004, http://www.cryomech.com/products.php?item_type=2

[3] Carlson, D.M. Sullivan, D.C. Bach, R.E. Resnick, D.R., "The ETA 10 liquid-nitrogen-cooled supercomputer system," IEEE Transactions on Electronic Systems, vol. 36, no. 8, pp. 1404-1413, 1989

[4] Kryotech, Inc., www.kryotech.com

[5] Asetek, Inc., Vapochill Product, Accessed April 2004, http://www.vapochill.com/default.asp?showPage=startside.asp&param=sideid&myvalue=14&contentSection=2&menuID=-1

[6] Carrier Inc., www.carrier.com

[7] Naemmi, A., "An upper limit for aggregate I/O interconnect bandwidth of GSI chips constrained by power dissipation", Proceedings of the IEEE 2004 International Interconnect Technology Conference, pp. 157-159, 2004.

[8] Schmidt, R.R., Notohardjono, B.D., "High-end low-temperature server cooling," IBM Journal of Research and Development, vol. 46, no. 6, pp. 739-751, Nov 2002

[9] Bowers, M.B., Mudawar, I., "Two-phase electronic cooling using mini-channel and micro-channel heat sinks: Part 2 - flow rate and pressure drop constraints," Journal of Electronic Packaging, Transactions of the ASME, vol. 116, 290-305, 1994

[10] Gillot, C., " Integrated Single and Two-Phase Micro Heat Sinks Under IGBT Chips," IEEE Trans. on Components and Packaging Technologies, vol. 22, no.3, 384-89, 1999

[11] Jiang, L., "Closed-loop electroosmotic microchannel cooling system for VLSI circuits," IEEE Transactions on Components and Packaging Technologies, 2002, vol. 25, no. 3, p 347-355

[12] Qu, W., Mudawar, I., "Measurement and correlation of critical heat flux in two-phase micro-channel heat sinks," International Journal of Heat and Mass Transfer, vol. 47, no. 10-11, pp. 2045-2059, 2003

[13] Kandlikar, S.G., Steinke, M.E., "High Speed photographic observation of flow boiling of water in parallel mini-channels," Proc. of 35th National Heat Transfer Conference, ASME, pp. 675-684, Anaheim, CA, 2001

[14] Wu, H.Y., Cheng, P., "Visualization and Measurements of periodic boiling in silicon microchannels," International Journal of Heat and Mass Transfer, vol. 46, pp. 2603-2614, 2003

[15] Carey, V.P., Liquid-Vapor Phase Change Phenomena, Hemisphere, 1992

[16] Kandlikar, S.G., "Two-phase flow patterns, pressure drop, and heat transfer during boiling in minichannel flow passages of compact evaporators," Heat Transfer Engineering, vol. 23, pp. 5-23, 2002

[17] Lee, J., Mudawar, I., "Two-phase flow in high-heat-flux micro-channel heat sink for refrigeration cooling applications: Part I-pressure drop characteristics", International Journal of Heat and Mass Transfer, vol. 48, pp. 928-940, 2005

[18] Lee, J., Mudawar, I., "Two-phase flow in high-heat-flux micro-channel heat sink for refrigeration cooling applications: Part II-heat transfer characteristics", International Journal of Heat and Mass Transfer, vol. 48, pp. 941-955, 2005

[19] Taitel, Y., Dukler, A.E., "A model for predicting flow regime transitions in horizontal and near horizontal gas-liquid flow," AIChE Journal, vol. 22, pp. 47-55, 1976

[20] Lockhart, R.W., Martinelli, R.C., "Proposed Correlation of Data for Isothermal Two-Phase, Two-Component Flow in Pipes," Chemical Engineering Progress, vol. 45, pp. 39-48

[21] Lee, H.J., Lee, S.Y., "Pressure drop correlations for two-phase flow within horizontal rectangular channels with small heights," International Journal of Multiphase Flow, vol. 27, pp. 783-796, 2001

[22]Kakac, Shah, Aung, "Handbook of Single-Phase Convective Heat Transfer," New York: Wiley, 1987

[23] Thome, J., Convective Boiling and Condensation, 3rd edition, Oxford University Press, 1994, pg. 106

[24] Schrock, V.E., Grossman, L. M., Forced convection boiling studies, Univ. of California, Institute of Engineering Research, Report no. 73308-UCX-2182, Berkeley, California, 1961

[25] Shah, M.M., Chart correlation for saturated boiling heat transfer: Equations and further study, ASHRAE Transactions, vol. 88, part 1, pp. 185-196, 1982

[26] Gungor, K.E., Winterton, R.H.S., A general correlation for flow boiling in tubes and annuli, International Journal of Heat and Mass Transfer, vol. 29, pp. 351-358, 1986

[27] Tran, T.N., Wambsganss, M.W., France, D.M., Small circular- and rectangular-channel boiling with two refrigerants, International Journal of Multiphase Flow, vol. 22, pp. 485-498, 1996

[28] Lee, H.J., Lee, S.Y., "Heat transfer correlation for boiling flows in small rectangular horizontal channels with low aspect ratios," International Journal of Multiphase Flow, vol. 27, pp. 2043-2062, 2001

[29] Warrier, G.R., Dhir, V.K., "Heat transfer and pressure drop in narrow rectangular channels, Experimental and Thermal Fluid Sciences, vol. 26, pp. 53-64, 2002